*J. Fluid Mech.* (2020), *vol*. 902, A13. © The Author(s), 2020.
Published by Cambridge University Press
doi:10.1017/jfm.2020.530



# Measurements of pressure and velocity fluctuations in a family of turbulent separation bubbles

**Arnaud Le Floc'h[1], Julien Weiss[1,2,†], Abdelouahab Mohammed-Taifour[1] and Louis Dufresne[1]**

[1]Laboratoire de thermo-fluide pour le transport, École de technologie supérieure, Montréal, Québec H3C 1K3, Canada

[2]Institute of Aeronautics and Astronautics, Technical University of Berlin, 10587 Berlin, Germany

(Received 24 December 2019; revised 16 April 2020; accepted 22 June 2020)

Measurements of wall-pressure and velocity fluctuations are performed in a family of three incompressible, pressure-induced, turbulent separation bubbles (TSBs) of varying sizes, with an emphasis on the energetic low and medium frequencies. In all three cases the streamwise distribution of wall-pressure fluctuations shows a bi-modal character, with a first local maximum close to the position of maximum adverse pressure gradient and a second local maximum at the very end of the region of intermittent back flow. The first maximum is shown to be caused by the superposition of two separate phenomena occurring at approximately the same streamwise position: first, the pressure signature of a low-frequency contraction and expansion (breathing) of the TSBs, whose amplitude is shown to increase with the size of the separation bubble, and second, the effect of the adverse pressure gradient on the turbulent structures responsible for the pressure fluctuations in the attached boundary layer. The second maximum of the wall-pressure fluctuation coefficient also increases with the size of the TSB and is associated with the convection of large structures within the shear layer. Possible scaling laws are examined to show that both the local maximum Reynolds shear stress $-\rho\overline{u'v'}_{max}$ and the local maximum wall-normal stress $\rho\overline{v'v'}_{max}$ are adequate to scale the pressure fluctuations along the TSBs, with a better match when low frequencies are removed. Furthermore, a comparison with existing data from the literature illustrates the effects of Reynolds number and TSB size on the wall-pressure and velocity fluctuations. Finally, measurements in the spanwise direction demonstrate that, although corner effects strongly distort the average flow, the scaling of wall-pressure fluctuations with the turbulent stresses remains relatively unaffected. The present results provide new insights into the unsteady character of pressure-induced turbulent separation bubbles and their associated wall-pressure fluctuations.

**Key words:** boundary layer separation, turbulent boundary layers

## 1. Introduction

When a two-dimensional turbulent boundary layer separates from a smooth surface because of an adverse pressure gradient and reattaches further downstream, it creates

† Email address for correspondence: julien.weiss@tu-berlin.de

a closed turbulent separation bubble (TSB). Such pressure-induced TSBs, which differ somewhat from the geometry-induced separation bubbles occurring when the boundary layer separates because of a sharp corner, feature several interesting characteristics like smooth-surface flow separation, significant wall-pressure fluctuations or low-frequency unsteadiness that make them relevant for fundamental fluid-dynamics research.

In practical flows, the adverse pressure gradient required to separate the boundary layer may be caused by surface curvature, flow deceleration and/or compressibility effects (shocks). Typical examples of TSBs generated by these processes include the flow around turbine blades (Patrick 1987), slowly expanding diffusers (Kaltenbach *et al.* 1999) and sufficiently strong shock/boundary-layer interactions (Delery 1985). There is also a significant amount of research, including the present work, concerned with the case of an incompressible, zero-pressure-gradient (ZPG), flat-plate turbulent boundary layer that eventually separates because of an imposed adverse pressure gradient (APG). The main advantage of such a configuration is its simplicity, inasmuch as it allows the separation process to establish itself freely on the flat surface, driven solely by the extent and amplitude of the APG, and without any influence of surface curvature or compressibility. Typically, existing research on flat-plate, pressure-induced TSBs either use a suction-only set-up on the wall opposite the test surface to create a local adverse pressure gradient that detaches the boundary layer which then reattaches naturally further downstream, or a suction-and-blowing condition to force reattachment. The former case was for example investigated in the experiments of Dianat & Castro (1989, 1991), Dengel & Fernholz (1990), Driver (1991), Alving & Fernholz (1996) and Angele & Muhammad-Klingmann (2006), who were mostly interested in the structure and scaling of turbulence through the adverse pressure gradient, and in the direct numerical simulation (DNS) of Skote & Henningson (2002), who investigated scaling laws near the wall in separation bubbles generated by two different APGs.

Among those experimentally using a suction-and-blowing condition, Perry & Fairlie (1975) devised a simplified calculation method for smooth flow separation, Patrick (1987) performed detailed turbulence measurements with the aim of improving Reynolds-averaged Navier–Stokes (RANS) turbulence models and Mohammed-Taifour & Weiss (2016) investigated low- and medium-frequency unsteadiness in the pressure and velocity fields of their TSB. From the mid-1990s, a significant number of numerical simulations were also performed using suction-and-blowing boundary conditions to detach and reattach a turbulent boundary layer. Spalart & Coleman (1997) used DNS to investigate the distribution of Reynolds stresses in a TSB with heat transfer in order to better evaluate RANS turbulence models. At around the same time, Na & Moin (1998*a*,*b*) reported the distribution of Reynolds stresses and coherent structures within a DNS-generated TSB. More recently, Raiesi, Piomelli & Pollard (2011) used DNS and large-eddy simulations (LES) of a separation bubble to evaluate the performance of common turbulence models, and Cheng, Pullin & Samtaney (2015) developed a virtual wall model for LES of separation and reattachment and validated it by numerically reproducing the experiments of Perry & Fairlie (1975) and Patrick (1987). The scaling of wall-pressure fluctuations in separation bubbles at different Reynolds numbers and sizes was investigated by Abe (2017) using DNS, while Wu & Piomelli (2018) concentrated on the effects of wall roughness within a TSB using LES. Finally, Coleman, Rumsey & Spalart (2018) extended the DNS of Spalart & Coleman (1997) from $Re_\theta \simeq 500$ up to $Re_\theta \simeq 3000$ (where $Re_\theta$ is the Reynolds number based on the velocity in the potential flow and the boundary-layer momentum thickness) and tested the accuracy of current RANS turbulence models.

Among those authors, only Na & Moin (1998*b*), Abe (2017), and Mohammed-Taifour & Weiss (2016) specifically investigated wall-pressure fluctuations in pressure-induced TSBs. Na & Moin (1998*b*), using DNS data obtained at $Re_\theta \simeq 300$, noted that wall-pressure fluctuations are increased in the separation and reattachment region but reduced within the separation bubble. They also showed that energetic pressure fluctuations in the TSB are associated with large-scale roller-type structures that convect at a speed of approximately $0.33U_{ref}$, where $U_{ref}$ is the incoming velocity in the potential flow. Abe (2017) increased the Reynolds number with a DNS at $Re_\theta \simeq 900$ and generally corroborated Na & Moin's (1998*b*) earlier results. The bi-modal distribution of pressure fluctuations, with a first peak of the fluctuating pressure coefficient $c_{p'} = 2p_{rms}/\rho U_{ref}^2$ near separation and a second peak near reattachment, was confirmed (here, $p_{rms}$ is the root mean square of the wall-pressure fluctuations and $\rho$ is the fluid density). The drop in $c_{p'}$ observed near the middle of the separation bubble was attributed to the negative production rate of turbulent kinetic energy (TKE) at the top of the shear layer, which is caused by the switch between APG and FPG in a suction-and-blowing transpiration profile (see also the corresponding discussion in Coleman *et al.* (2018)). Furthermore, both the first and second peaks of $c_{p'}$ appear to depend on the size of the TSB and consequently on the exact streamwise pressure distribution and transpiration profile. Abe (2017) also investigated the scaling of pressure fluctuations with Reynolds shear and wall-normal stresses and showed consistency with the results of Simpson, Ghodbane & McGrath (1987) and Na & Moin (1998*b*) near detachment ($p_{rms}/-\rho\overline{u'v'}_{max} \simeq 2.5$–$3$) as well as with those of Ji & Wang (2012) near reattachment ($p_{rms}/\rho\overline{v'v'}_{max} \simeq 1.2$).

The experimental work of Weiss, Mohammed-Taifour & Schwaab (2015) and Mohammed-Taifour & Weiss (2016) in a large pressure-induced TSB at $Re_\theta \simeq 5000$ specifically concerned the unsteady behaviour of the flow, as quantified by measurements of both wall-pressure and velocity fluctuations. In these two articles, the authors showed that a TSB is subject to unsteadiness in a broad range of frequencies. At low frequency ($St = fL_b/U_{ref} \simeq 0.01$, where $St$ is the Strouhal number, $f$ is the frequency and $L_b$ the size of the bubble defined as the distance between transitory detachment and transitory reattachment (Simpson 1989)), the TSB appears to expand and contract in a quasi-periodic breathing motion. This motion was educed using a pair of classical thermal-tuft probes in Weiss *et al.* (2015) and later confirmed by high-speed particle image velocimetry (PIV) measurements in Mohammed-Taifour & Weiss (2016). At a medium normalized frequency of $St \simeq 0.35$, the unsteady behaviour of the flow is characterized by roller-like structures similar to those observed in the DNSs of Na & Moin (1998*b*) and Abe (2017), and with a very close convection velocity of $U_c \simeq 0.30U_{ref}$. Finally, at higher frequencies ($St > 1$), the pressure and velocity fluctuations are caused by the turbulent nature of the flow. Mohammed-Taifour & Weiss (2016) also observed a bi-modal distribution of the pressure fluctuations, with a first peak of $c_{p'}$ near detachment and a second near reattachment, but attributed the first peak to the low-frequency breathing motion of the TSB (see also Weiss *et al.* (2015)). This appears to be inconsistent with the results of Na & Moin (1998*b*) and Abe (2017) who also observed a first peak of $c_{p'}$ near detachment but did not resolve the low-frequency breathing motion near $St \simeq 0.01$ because of the necessarily limited simulation time of their DNS.

In a recent contribution, Wu, Meneveau & Mittal (2020) compared the spatio-temporal dynamics of TSBs generated by either suction-and-blowing or suction-only boundary conditions via DNS. They confirmed the presence of a low-frequency breathing motion in a very long TSB generated with the suction-only set-up but not in the smaller TSB obtained using the suction-and-blowing condition. Furthermore, they associated this unsteadiness with a flow topology dominated by highly elongated structures in the streamwise direction,

which may be linked to a Görtler instability induced by the streamwise curvature on the upstream end of their long TSB. These new results suggest that the size and structure of a TSB has a strong influence on its low-frequency unsteadiness, which is consistent with the work of Le Floc'h, Mohammed-Taifour & Weiss (2017) that indicated a possible influence of the amount of mean back flow on the amplitude of the breathing.

Hence, the first objective of the present contribution is to investigate the effect of the TSB size on its low- and medium-frequency unsteadiness. This will be done by comparing the pressure and velocity fluctuations measured in two new pressure-induced TSB flows (a small TSB, which does not feature any mean back flow, and a medium-sized one, which does) to those obtained in the large-scale TSB of Mohammed-Taifour & Weiss (2016). The choice of a small TSB which is attached in the mean but still features large regions of instantaneous back flow was deliberate, so as to investigate if the low- and medium-frequency unsteadiness that was observed so far in large TSBs still occurs without any mean detachment. Our second objective is to clarify the cause of the local maximum in wall-pressure fluctuations that occurs upstream of the mean separation in the numerical simulations of Na & Moin (1998*b*) and Abe (2017), and in the experiments of Weiss *et al.* (2015) and Mohammed-Taifour & Weiss (2016). Of particular interest would be to know if this local maximum is the result of the APG imposed on the attached turbulent boundary layer, as suggested by the simulations, or if it is caused by the low-frequency breathing motion. Finally, our third objective is to investigate experimentally the scaling of pressure fluctuations with Reynolds stresses for the three TSBs, in an attempt to corroborate the results obtained earlier in the numerical simulations of Na & Moin (1998*b*) and Abe (2017). The existence of such a scaling would provide a convenient way to estimate Reynolds stresses from pressure fluctuation measurements or, *vice versa*, to estimate pressure fluctuations from Reynolds stresses obtained by, say, engineering RANS simulations. Note that Simpson *et al.* (1987) suggested that the maximum turbulent shear stress $-\rho\overline{u'v'}_{max}$ is the proper stress on which to scale the wall-pressure fluctuations $p_{w\ rms}$ in a separating turbulent boundary layer, while Ji & Wang (2012) found a scaling with the wall-normal stress $\rho\overline{v'v'}_{max}$ more satisfactory, specifically for turbulent reattaching flows.

Of relevance to the present study is a discussion of the three-dimensional nature of average pressure-induced TSBs. While numerical simulations invariably use periodic or no-slip boundary conditions in the spanwise direction in order to generate a nominally two-dimensional average flow, experimental investigations of pressure-induced TSBs are known to be strongly affected by wind-tunnel sidewalls. Except in the relatively rare cases of axisymmetric test sections (Driver 1991; Alving & Fernholz 1996), these walls necessarily generate secondary flows that affect the average separation bubble. This can be particularly problematic when the experiments are used as a validation case for computational fluid dynamics (CFD). In an asymmetric diffuser flow, for example, Buice & Eaton (1995) and Kaltenbach *et al.* (1999) describe how the experiments of Obi, Aoki & Masuda (1993) did not satisfy the conservation of mass on the wind-tunnel centreline, which is indicative of an average out-of-plane velocity component most likely caused by asymmetric separated zones on each sidewall (Buice 1997). This prevented a satisfactory comparison between RANS computations and experiments. In flat-plate TSB flows, most investigators so far have only briefly reported the occurrence of three-dimensional effects. Patrick (1987) used corner suction to improve the two-dimensionality of the flow near the test surface and reported, based on limited visualizations of injected dye streaks, that the mean separation line was angled at 7° with respect to the perpendicular to his tunnel centreline, which corresponds to ±6 % of the span. Perry & Fairlie (1975) used glass spheres as surface tracers to draw a simplified topological map of their separation bubble but noted that the actual near-wall flow pattern would be

further complicated by corner eddies. Mohammed-Taifour & Weiss (2016) successfully used oil-film visualizations to draw a consistent topological map of the skin-friction lines in their test section. They showed the strongly three-dimensional nature of the near-wall flow but argued that wall-normal measurements near the centreline can be considered as quasi-two-dimensional. Based on our recent experience and the results of others, e.g. Simmons, Thomas & Corke (2019), we believe that a truly two-dimensional pressure-induced TSB is all but impossible to generate in a rectangular test section. The degree of three-dimensionality must therefore be assessed and put in perspective with the experiment's objectives.

This article is organized as follows. In § 2, the experimental apparatus and the different flow cases are presented. In particular, the average wall-pressure distributions and the vertical velocity profiles used to generate the separation bubbles are compared to those already published in the literature. Experimental results are then discussed in § 3: the general flow topology is presented in § 3.1, with a specific emphasis on three-dimensional effects in the mean flow. Sections 3.2 and 3.3 discuss the pressure statistics and their scaling with Reynolds stresses on the wind-tunnel's centreline, while § 3.4 investigates the effect of mean-flow three-dimensionality on the pressure and velocity fluctuations. Finally, a conclusion is offered in § 4.

## 2. Experimental apparatus

### 2.1. *Wind tunnel and flow cases*

Experiments were performed in the TFT boundary-layer wind tunnel already described in detail in Mohammed-Taifour *et al.* (2015) and Mohammed-Taifour & Weiss (2016). Briefly, the low-speed wind tunnel is of blow-down type, with a test section 3 m in length and 0.6 m in width, as illustrated in figure 1. In the first half of the test section, a ZPG boundary layer develops on the upper surface and separates because of the APG imposed by the diverging test-section floor. The boundary layer subsequently reattaches due to the FPG that occurs when the floor converges again. The use of a bleed slot ensures that the boundary layer on the lower surface stays attached on the contoured part of the test-section floor. This slot connects directly to the atmosphere, while the interior of the test section is maintained at a slightly elevated pressure by a mesh positioned at the exit.

As shown in figure 1, the diverging test-section floor generates a strong adverse pressure gradient starting at about $x \simeq 1.4$ m, where $x = 0$ marks the entrance of the test section. The original geometry of the test-section floor creates the pressure distribution depicted with black squares, as already investigated by Mohammed-Taifour & Weiss (2016). In the present work, a set of two foam blocks are inserted in the aft part of the contoured test-section floor so that the APG stays the same but two new zones of FPG are created more upstream of the original geometry, thereby generating two new separation bubbles of smaller sizes. The contour depicted with the blue dashed line in the lower part of figure 1 creates a $c_p$ distribution for the 'Small TSB', while the one with the red dash-dot line creates a pressure distribution for the 'Medium TSB'. The original $c_p$ distribution of Mohammed-Taifour & Weiss (2016) results in a 'Large TSB'. Note that $c_p(x) = 2(p(x) - p_{ref})/\rho U_{ref}^2$, where $p_{ref}$ and $U_{ref}$ refer to the static pressure and velocity at the entrance of the test section, respectively (details regarding the instrumentation used in the wind tunnel are given in § 2.2). For all experiments, the reference velocity is $U_{ref} = 25$ m s$^{-1}$ and the atmospheric air density is $\rho \simeq 1.2$ kg m$^{-3}$. Also, at $x_{in} = 1.1$ m the incoming boundary-layer thickness is $(\delta_{99})_{in} = 28$ mm and the momentum thickness is $\theta_{in} = 3.0$ mm, which implies a Reynolds number $Re_{\theta_{in}} \simeq 5000$, as in Mohammed-Taifour & Weiss (2016).

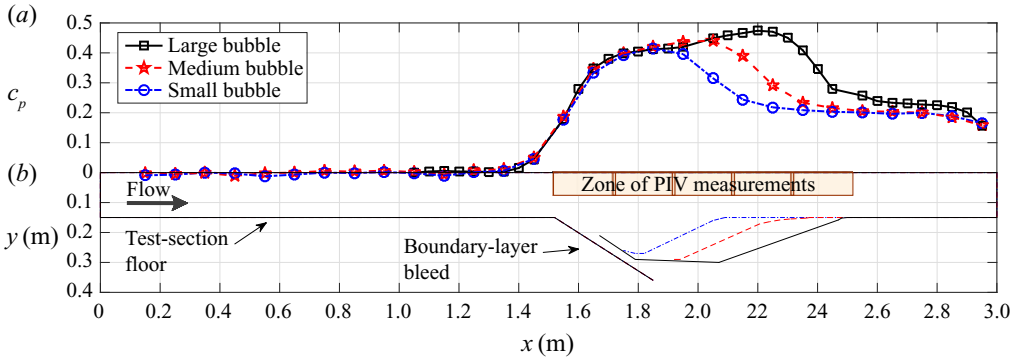


FIGURE 1. (*a*) Average wall-pressure coefficient $c_p$ measured on the test-section centreline ($z = 0$ m) along the streamwise axis. (*b*) Profile sketch of the test section. The black solid line corresponds to the Large TSB of Mohammed-Taifour & Weiss (2016), the red dashed line is the new Medium TSB and the blue dash-dotted line is the new Small TSB.

The pressure distributions generated experimentally in the TFT Boundary-Layer Wind Tunnel are compared to those obtained by other researchers in figure 2, with relevant data also listed in table 1. The available database consists of the experimental results of Perry & Fairlie (1975) and Patrick (1987), as well as the CFD results of Na & Moin (1998*a*), Abe (2017), Coleman *et al.* (2018) (noted CRS) and Wu & Piomelli (2018). In order to provide a meaningful comparison, a common datum is required to position the different pressure distributions. Following Coleman *et al.*'s (2018) suggestion, the streamwise position $x_{V_{top}=0}$ where the transpiration profile changes sign from suction to blowing was chosen as a common reference since it can easily be obtained from all published data, except for the experiment of Perry & Fairlie (1975), where the calculated transpiration profile of Cheng *et al.* (2015) was used instead. For the present data and those of Patrick (1987), $x_{V_{top}=0}$ was defined by using the vertical velocity measured furthest away from the test surface as a proxy for the transpiration profile. The streamwise position was furthermore normalized by the momentum thickness $\theta_0$ that the ZPG boundary layer would reach at $x_{V_{top}=0}$ in the absence of any pressure gradient. This value was calculated from the published data by integrating the von Kármán integral equation $\mathrm{d}\theta/\mathrm{d}x = c_f/2$ from its value $\theta_{in}$ at a specified ZPG position in the original publication to its value $\theta_0$ at $x_{V_{top}=0}$ (for the present experiments the reference streamwise position is $x_{in} = 1.1$ m). The classical ZPG power law $c_f/2 = 0.0128Re_\theta^{-0.25}$, from Schlichting (1968, p. 600), was used in the integration. The Reynolds numbers $Re_{\theta_{in}}$ at each reference position and the corresponding $Re_{\theta_0}$ at each $x_{V_{top}=0}$ are listed in table 1, where it can be seen that, depending on the choice of reference position in the original article, $Re_{\theta_0}$ can be as much as twice $Re_{\theta_{in}}$.

Several noteworthy features can be observed in figure 2. First, most of the $c_p$ distributions show the classical bell-shaped form expected from a suction-and-blowing transpiration profile. Notable exceptions are those obtained in the present work, which do not go back down to $c_p = 0$ after reattachment. This is due to the geometry of the wind-tunnel test section, which has the same height upstream and downstream of the pressure-gradient zone. Bringing $c_p$ down to zero would require a smaller height in the aft part to compensate for the mass flow removed by the bleed slot (approximately 10 % of the incoming mass flow, corresponding to $c_p \simeq 0.2$). The same can be said from the pressure distribution of Patrick (1987), who used a similar experimental set-up. The third exception is the pressure distribution from Perry & Fairlie (1975), which features a mild APG starting much earlier than the others, and a very strong FPG to close the bubble.

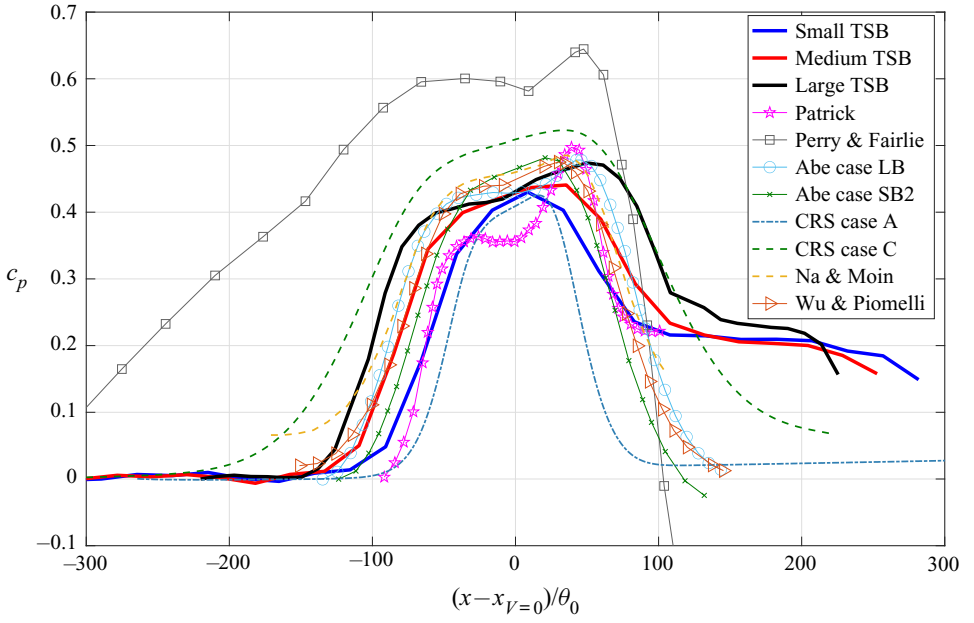


FIGURE 2. Streamwise distributions of wall-pressure coefficient.

| Reference | $Re_{\theta_{in}}$ | $Re_{\theta_0}$ | $\frac{H_{V_{top}}}{\theta_0}$ | $\frac{L_b}{\theta_0}$ | $\frac{L_p}{\theta_0}$ | $\frac{H_b}{L_b}$ | $\frac{w}{L_p}$ | $\left[\frac{V_{top}}{U_{ref}}\right]_{max}$ | [APG] | [FPG] |
|---|---|---|---|---|---|---|---|---|---|---|
| | | | | | Experimental | | | | | |
| Perry & Fairlie | 2000 | 4404 | n/a | 121 | 284.3 | 0.19 | 0.61 | n/a | 2.2 | −18 |
| Small TSB* | 5000 | 6711 | n/a | n/a | 114.2 | n/a | 1.30 | n/a | 6.6 | −3.8 |
| Medium TSB* | 5000 | 6905 | n/a | 26.6 | 154.5 | 0.06 | 0.94 | n/a | 6.9 | −4.6 |
| Large TSB* | 5000 | 7107 | n/a | 93.8 | 192.3 | 0.12 | 0.73 | n/a | 7.1 | −5.9 |
| Patrick | 11 100 | 13 172 | n/a | 64.6 | 116.7 | 0.31 | 0.99 | n/a | 12.5 | −12.2 |
| | | | | | Numerical | | | | | |
| Na & Moin | 300 | 601 | 53.2 | 84.9 | 158.6 | 0.13 | 0.26 | 0.53 | 6.8 | −7.1 |
| Abe case SB2 | 300 | 465 | 51.5 | 45.1 | 123 | 0.053 | 0.84 | 0.43 | 7.0 | −7.4 |
| Abe case LB | 900 | 1291 | 56.1 | 96.1 | 159 | 0.19 | 0.71 | 0.52 | 7.9 | −8.0 |
| CRS case A | 1035 | 1437 | 27.8 | 35.6 | 86 | 0.093 | 1.29 | 0.40 | 9.4 | −10.2 |
| CRS case C | 1744 | 3121 | 25.6 | 33.3 | 207.5 | 0.033 | 0.49 | 0.13 | 5.0 | −4.8 |
| Wu & Piomelli | 2500 | 3367 | 52.0 | 61.6 | 142.6 | 0.16 | 0.28 | 0.52 | 6.9 | −7.6 |

TABLE 1. Definition of the main pressure-induced TSB features: data with (*) are from the present study; CRS stands for Coleman *et al.* (2018); $\theta_{in}$ and $\theta_0$ are the momentum thicknesses at the reference position and $x_{V_{top}=0}$, respectively; $V_{top}$ is the transpiration profile imposed in numerical simulations and $H_{V_{top}}$ its height above the wall; $L_b$ is the distance between transitory detachment (TD) and transitory reattachment (TR); $L_p$ is the distance between the maximum APG and FPG; $H_b$ is the maximum distance between the mean dividing streamline and the wall; $w$ is the width of the test section for experimental data and the spanwise extent of numerical domains; finally, [APG] and [FPG] are defined as $\theta_0 \cdot [\mathrm{d}C_p/\mathrm{d}x]_{max} \times 10^{-3}$ and $\theta_0 \cdot [\mathrm{d}C_p/\mathrm{d}x]_{min} \times 10^{-3}$, respectively.

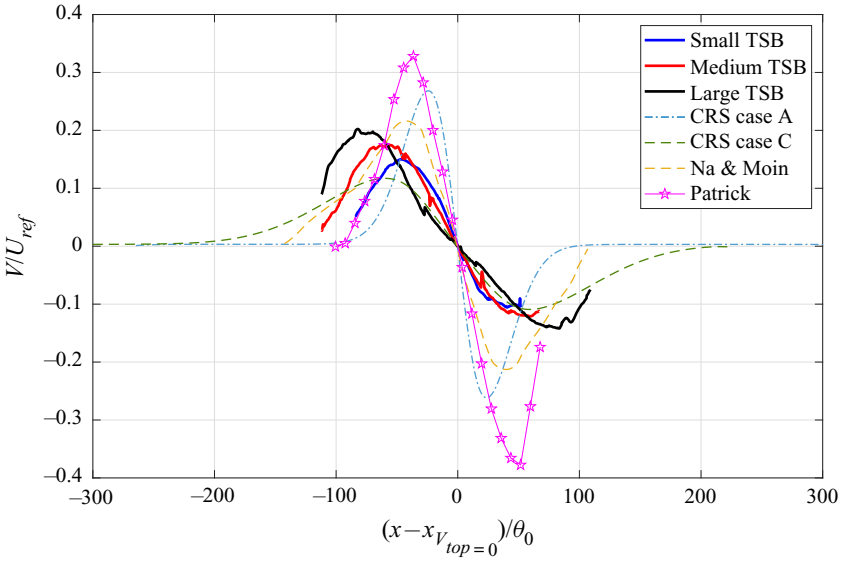


FIGURE 3. Streamwise distributions of vertical velocity at $y/\theta_0 \simeq 17$. The data from Na & Moin (1998*a*) were interpolated from their figure 19.

The Patrick (1987) pressure distribution also stands out because of its clear apex in the downstream half of the bell-shaped curve, which is interpreted in his original report as the result of the impingement and partial stagnation of the reattaching flow. A similar feature, albeit at a more modest scale, can be seen in most other cases. Table 1 lists the wall-normal aspect ratios of the separation bubbles, defined as the height $H_b$ of the recirculation zone divided by its length $L_b$, where $H_b$ is the maximum distance between the wall and the mean dividing streamline, whereas $L_b$ is the distance between transitory detachment and reattachment. Comparing this parameter with the $c_p$ curves of figure 2 reveals that the peak in the pressure distribution is more pronounced for larger wall-normal aspect ratios. This is consistent with the Patrick (1987) explanation of impingement being responsible for the pressure peak, though the large Reynolds number in his case might also play a significant role.

Generally speaking, except for Perry & Fairlie (1975), most $c_p$ distributions appear to cluster between the Coleman *et al.* (2018) cases A and C. The pressure distributions from Na & Moin (1998*a*), Abe (2017) (case LB) and Wu & Piomelli (2018) are very close, mostly because the latter authors designed their simulations to reproduce Na and Moin's results. The Coleman *et al.* (2018) case A has comparable pressure gradients but imposed on a shorter distance. In contrast, their case C imposes smaller gradients but over a larger distance. The Patrick (1987) distribution appears shorter, although it can be seen as an artefact caused by the larger Reynolds number that results in a larger $\theta_0$. Finally, the pressure distributions generated in the TFT Boundary-Layer Wind Tunnel appear to have APGs reasonably close to Na & Moin (1998*a*) and others, whereas our FPGs are closer to the Coleman *et al.* (2018) case C (see also the maximum APG and FPG listed in table 1 for each case).

To provide further insight into the different flow cases, the normalized vertical velocity $V/U_{ref}$ measured at the edge of our experimental field of view ($y/\theta_0 \simeq 17$) is plotted in figure 3 as a function of the normalized streamwise distance. Only the velocity data from Na & Moin (1998*a*), Coleman *et al.* (2018) and Patrick (1987) were available for

comparison at $y/\theta_0 \simeq 17$. The main interesting feature of figure 3 is that, in contrast to the present data, all available flow cases are approximately symmetrical, with the same amplitudes for suction and blowing. However, the data obtained in the TFT wind tunnel exhibit a larger amplitude in the suction part ($V > 0$) than in the blowing part ($V < 0$), which is consistent with the fact that the FPG is smaller than the APG (see table 1 and figure 2). Furthermore, the suction velocity in our Large TSB appears to be fairly close to that of Na & Moin (1998*a*), but significantly smaller than in the Patrick (1987) flow. On the other hand, the blowing velocity of our Medium TSB is very close to the Coleman *et al.* (2018) case C. This compilation of velocity data is fully consistent with the pressure distributions of figure 2.

Based on a comparison of the normalized separation lengths $L_b/\theta_0$ and aspect ratios $H_b/L_b$ listed in table 1, and based on the pressure and velocity data from figures 2 and 3, we conclude that our Large TSB is probably geometrically closest to the Na & Moin (1998*a*) flow, despite a significant difference in Reynolds number. Similarly, our Medium TSB is probably the closest to the Coleman *et al.* (2018) case C, with a factor of approximately 2 in Reynolds number and a notable difference in pressure distribution. Of course, two TSB flows would only be identical if the Reynolds numbers and pressure distributions were identical, or equivalently if the Reynolds numbers were identical and the same transpiration profiles were imposed at the same wall-normal distance.

### 2.2. *Instrumentation*

The experimental techniques used in the present work were essentially the same as in Weiss *et al.* (2015) and Mohammed-Taifour & Weiss (2016) and will only be described briefly. The average wall pressure was measured using two Scanivalve DSA3217 pressure scanners and the wall-pressure fluctuations with several Meggitt 8507C-1 piezoresistive pressure transducers. The estimated uncertainty of the measured values is $\pm 0.7\,\%$ and $\pm 5\,\%$ for the mean and fluctuating pressure, respectively (Weiss *et al.* 2015). Necessary corrections of the fluctuating pressure data to remove the low-frequency facility noise caused by small mass-flow fluctuations from the flow mover were made by applying the noise-correction method of Weiss *et al.* (2015), which consists in removing the part of the signal that is coherent with the noise measured near the entrance of the test section. The forward-flow fraction $\gamma$, defined as the percentage of time that the near-wall flow goes in the main, positive streamwise direction, was measured with the MEMS calorimetric shear-stress sensor introduced by Weiss *et al.* (2017). The uncertainty in $\gamma$ was estimated at $\pm 2\,\%$ based on a comparison with the classical thermal-tuft probe of Schwaab & Weiss (2015). All single-point unsteady signals were digitized with a 24-bit National Instruments NI-PXIe-4492 data acquisition card at a sampling rate of 2 kHz and low-pass filtered with the embedded anti-aliasing filter. Power spectral densities were computed using Welch's modified periodogram algorithm with 50 % overlap and a Hamming window (Bendat & Piersol 2010).

The wall-pressure fluctuations were obtained by connecting the piezoresistive pressure transducers to pressure taps installed on the test surface with 15 mm long flexible tubing. This set-up resulted in an organ-pipe resonance frequency of approximately 2 kHz for the tube-and-pressure-tap system. Using the boundary-layer displacement thickness $\delta^* = 3.80$ mm measured at $x_{in} = 1.1$ m (ZPG) and the Nyquist frequency $f = 1$ kHz of the pressure signals, the maximum normalized frequency that can be resolved is $\omega\delta^*/U_{ref} = 0.95$, with $\omega = 2\pi f$. This value is lower than for dedicated acoustic measurements using pinholes (Simpson *et al.* 1987; Bull 1996). Thus, our pressure data are mainly concentrated within

the energetic low- and medium-frequency range observed under the turbulent separation bubbles and does not resolve the high-frequency fluctuations present under the attached incoming boundary layer (see also the discussion pertaining to figures 10 and 15).

Planar flow velocity measurements were achieved using a high-speed, planar, two-component (2D-2C), PIV system that consists of a Litron LDY304 Nd:YLF laser, light-sheet optics and two Phantom V9.1 CMOS cameras mounted side by side. Both cameras were equipped with a 50 mm, f#2 Micro Nikkor lens to obtain a total field of view of approximately 0.20 m in the streamwise direction and 0.075 m in the wall-normal direction. The pair of cameras was moved in the streamwise direction to cover the complete length of all the separation bubbles (see figure 1). Respectively three, four and six stations were required for the Small, Medium and Large TSBs. In the case of the Large TSB, a total of five separate sequences of 3580 images were recorded at a sampling frequency of 900 Hz, thus resulting in a total dataset spanning 20 s (Mohammed-Taifour & Weiss 2016). For the Small and Medium TSBs, in order to optimize the data storage requirements, three separate sequences of 3580 images were recorded at a reduced sampling frequency of 400 Hz for a total measuring time of 27 s. It was verified that the change of sampling frequency from 900 Hz to 400 Hz had no detrimental impact in capturing the flow statistics. The images were processed by the LaVision DaVis software (version 8.2) using a multi-pass correlation technique with 75 % overlap. The vector spacing in the object plane is 0.55 mm, which corresponds to approximately 2 % of the boundary-layer thickness at $x_{in} = 1.1$ m ($\delta_{99} = 28$ mm) and 13 % of $\theta_0$ ($\theta_0 \simeq 4.1$ mm).

In Mohammed-Taifour & Weiss (2016) the PIV data were validated by a favourable comparison with hot-wire results, both in the incoming ZPG boundary layer and in the large separation bubble. Rather than reproducing similar results, we show in figure 4 a comparison between the turbulence statistics $\bar{U}/U_{ref}$, $\overline{u'u'}/U_{ref}^2$, $\overline{v'v'}/U_{ref}^2$ and $-\overline{u'v'}/U_{ref}^2$ measured in our Medium TSB with the DNS results of the Coleman *et al.* (2018) case C. For both databases the $x$ axis was normalized by the distance $L_p$ between the maximum APG and the maximum FPG (also listed in table 1). Clearly, the results are rather close to one another, which is expected given the similarities in the bubble dimensions from table 1. While this favourable comparison gives confidence in the PIV data, it also shows the reduced spatial resolution and convergence of the PIV results compared to the DNS, which is a consequence of the limited resolution of the CMOS cameras, the required stitching between different fields of view and the limited integration time resulting from the finite camera memory. In order to estimate realistic uncertainty bounds for the PIV data, a detailed convergence study was performed on all measured turbulence statistics on a large number of grid points spanning the complete field of view. Specifically, the difference between the maximum and minimum value of the convergence curves over the last 30 % of the total measurement time was used as an estimate of the random uncertainty. Furthermore, the small step occurring at the boundary between two adjacent fields was quantified and used as an estimate of the systematic uncertainty. The total uncertainties estimated by this procedure are $\pm 0.2$ m s$^{-1}$ for the mean streamwise velocity, $\pm 0.3$ m s$^{-1}$ for the mean wall-normal velocity, $\pm 0.2$ m$^2$ s$^{-2}$ for the streamwise stresses, $\pm 0.1$ m$^2$ s$^{-2}$ for the wall-normal stresses and $\pm 0.1$ m$^2$ s$^{-2}$ for the shear stresses. This translates into relative uncertainties of approximately 1 % for the mean velocities (based on the inlet velocity $U_{ref} = 25$ m s$^{-1}$), and 4 %, 5 % and 10 % for the streamwise, wall-normal and shear stresses, respectively (based on the median stresses for the Medium TSB). These uncertainty estimates are typical of current high-speed PIV systems, e.g. Ma, Gibeau & Ghaemi (2020). Nevertheless, the proximity of the test surface or unavoidable reflections from the test-section walls may locally generate larger errors.

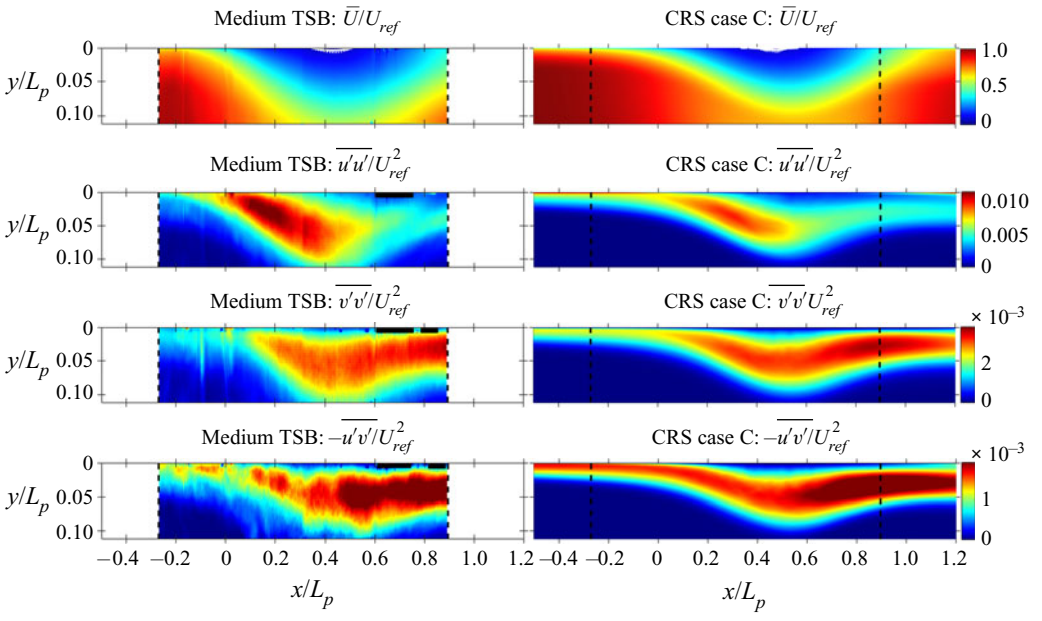


FIGURE 4. Medium TSB (left) compared with the Coleman *et al.* (2018) case C (right). Black squares hide invalid PIV data in some near-wall regions.

## 3. Experimental results

### 3.1. *General flow topology*

Oil-film visualizations on the test surface for the three separation bubbles are shown in figure 5. The oil film was a mixture of titanium dioxide, paraffin oil and some oleic acid that was applied on the surface before turning on the wind tunnel. The images show the complete span of the test section (0.6 m) and a streamwise distance of 1 m that approximately corresponds to the region of imposed pressure variations for the Large TSB (compare with the axis system defined in figure 1). The non-dimensional spanwise axis $z^* = z/z_0$, with $z_0 = 0.30$ m corresponding to the half-span of the test section, is also introduced. Iso-$\gamma$ lines of constant forward-flow fraction are superimposed on the images. These lines were obtained by interpolating the values of the forward-flow fraction $\gamma$ measured with the calorimetric shear-stress sensor on a raster of 10 cm × 10 cm on the test surface.

The general topology of the surface streamlines appears to be reasonably similar for all separation bubbles. In all cases, the flow is symmetric with regard to the centreline. The limiting streamlines are essentially straight in a narrow slice which spans a third of the test-section width for the Medium and Large TSBs (i.e. $|z^*| < 1/3$) and approximately half its width for the Small TSB ($|z^*| < 1/2$). Outside of this central range, strong three-dimensional effects caused by the complex flow near the corners of the test section are evident, although flow visualizations on the sidewalls did not indicate any mean separation from the sidewall boundary layers (Mohammed-Taifour & Weiss 2016). The iso-$\gamma$ lines are consistent with the oil-film images and, although slightly curved, do not show any strong asymmetry in the near-wall flow. Surprisingly, although the ratio between mean separation length and test-section span is smaller for the Medium TSB than for the Large TSB, the size of the region affected by the corner flows is relatively similar.

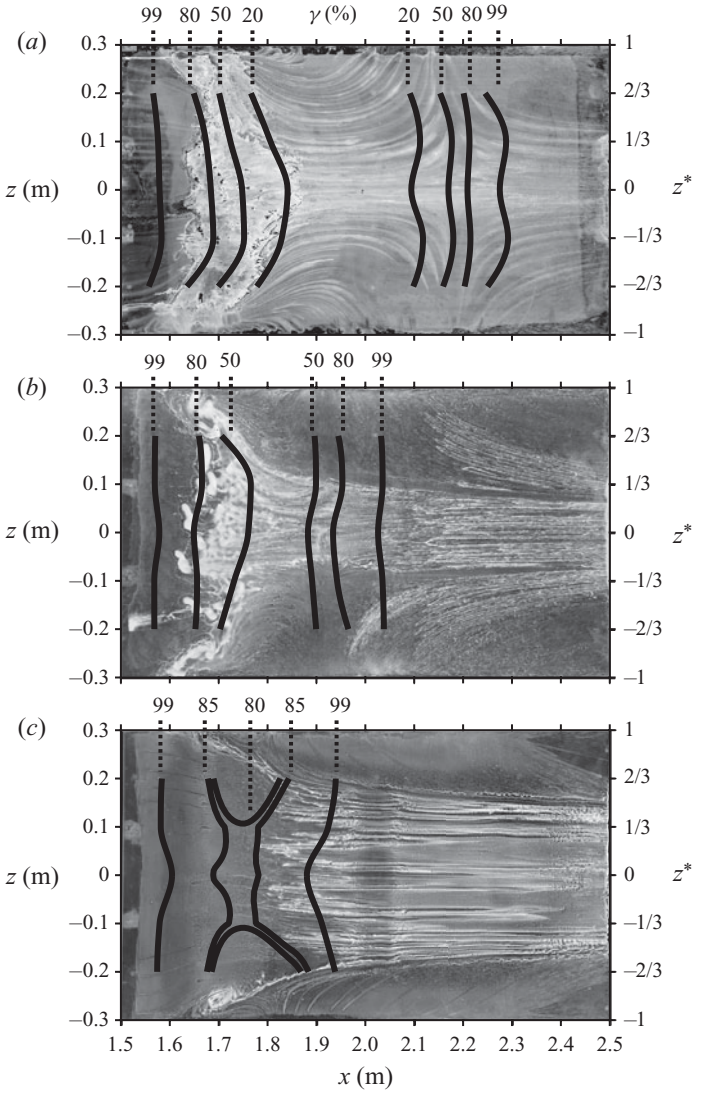


FIGURE 5. Oil flow visualizations of the three separation bubbles. (*a*) Large TSB. (*b*) Medium TSB. (*c*) Small TSB. Black lines: forward-flow fraction $\gamma$.

This indicates that, proportionally to the TSB length, the three-dimensional effects are more pronounced for the Medium TSB.

The symmetry of the shear-stress lines on the test surface necessarily precludes any significant mean out-of-plane velocity component on the test-section centreplane, as those wall streamlines are exceedingly sensitive to minute transverse pressure gradients. In that respect, the flow near the centreline can be described as quasi two-dimensional in the mean. Nevertheless, it should be emphasized that the average flow near the centreline is not necessarily the same as the flow that would be obtained if the test-section width was infinite. In a geometry-induced TSB created with a fence and splitter plate, Ciampoli & Hancock (2006) found that residual effects of the tunnel sidewalls are seen in the mean wall shear stress near the tunnel centreline up to a test-section width to bubble length

ratio of approximately 7. This is much larger than any experiment performed so far on pressure-induced TSBs (see table 1, where $w/L_p$ is typically of the order of one). Hence, our mean TSBs are necessarily affected by the presence of the sidewalls, even near the centreline.

Because three-dimensional flow structures can only be crudely hypothesised from two-dimensional oil-film visualizations, a qualitative RANS simulation of the Medium TSB was performed using a commercial CFD software (ANSYS CFX-17.2) in order to better understand the three-dimensional nature of the average flow. The complete wind-tunnel test section was discretized with a standard hexahedral mesh composed of 20 million cells that was refined near the walls to achieve a first node value of $y^+ < 1$. The model boundaries consisted of the test-section inlet and exit, the two side walls, the ceiling and floor walls, and the boundary-layer bleed. The test-section length was extended near its entrance to match the experimental boundary-layer thickness at $x_{in} = 1.1$ m and the inlet boundary condition was set at an average velocity of $U_{ref} = 25$ m s$^{-1}$ and a turbulence level of 0.05 %, as measured experimentally (Mohammed-Taifour *et al.* 2015). Both the boundary-layer bleed and the test-section exit outlet conditions were set at zero gradient, and the imposed pressures were chosen by trial and error in order to reproduce as closely as possible the experimental $c_p$ distribution of figure 1. Grid convergence was deemed satisfactory based on a comparison of results obtained on three grid sizes composed of 9 (coarse), 20 (medium) and 44 (fine) million cells. Several turbulence models were tested and the BaSeLine Explicit Algebraic Reynolds Stress Model (BSL-EARSM) described in Menter, Garbaruk & Egorov (2012) was finally selected because it best reproduced the wall streamlines visualized experimentally (Mohammed-Taifour, Dufresne & Weiss 2019).

The results of the simulation should only be interpreted *qualitatively* because it is well known that RANS methods are not capable of accurately reproducing many quantitative aspects of turbulent separated flows (Coleman *et al.* 2018). Nevertheless, the three-dimensional structure of the simulated average flow presented in figure 6 shows several noteworthy features that help interpret the experimental wall streamlines: First, the simulated shear-stress lines on the top surface suitably reproduce the oil-film visualization of figure 5, thereby bringing credibility to the RANS results. Second, the distinction between a central zone with approximately straight shear-stress lines and two symmetrical zones with strong three-dimensional effects for $|z| > 0.1$ m, already apparent on the oil film, is also evident in figure 6. Finally, the RANS results clearly show that the three-dimensional nature of the wall streamlines on the top surface is not caused by separation from the sidewall boundary layers (as also verified experimentally), but rather by the signature of large-scale, longitudinal corner vortices that create a spanwise velocity component oriented towards the centreline close to the test surface. The generation of these corner vortices can be interpreted by classical secondary-flow arguments (Bradshaw 1987): the curvature of the streamlines in the potential flow imposes a lateral pressure gradient on the sidewall boundary layers (i.e. in the $y$-direction). In the upstream half of the separated region, the cross-flow profiles are directed towards positive $y$, away from the test surface. On the other hand, in the downstream half of the TSB, the cross-flow profiles are oriented towards the test surface. This translates into an upward motion of the lateral boundary layers, which flow around the corners towards the centreline of the test surface. Moving downstream, this flow pattern rolls up into two large longitudinal corner vortices. In many ways this phenomenon is reminiscent of the streamwise vortices observed in constant width wind-tunnel contractions (Mokhtari & Bradshaw 1983; Bouriga *et al.* 2015). In the remainder of this section we will consider experimental data obtained on the test-section centreline only, where quasi-two-dimensional conditions can be observed.

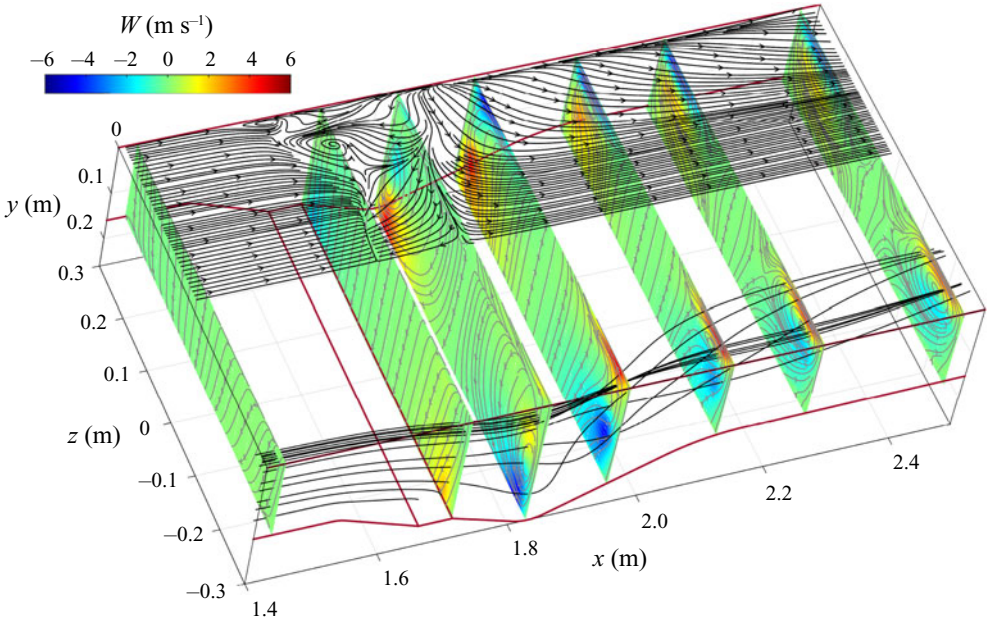


FIGURE 6. RANS simulation results showing the average flow structure in the Medium TSB. Black lines on top: wall streamlines on the left-hand side of the test surface. Coloured cuts: contours of the average spanwise velocity $\overline{W}$. Black lines on the bottom: representative streamlines showing the effects of the corner flow.

However, because of the three-dimensional character of the average flows discussed above, we will return to this point in § 3.4.

Looking back at figure 5, it can be observed that the forward-flow fraction has a constant value of $\gamma \simeq 100\,\%$ upstream of the field of view. The threshold $\gamma = 99\,\%$, corresponding to the position of incipient detachment (ID) according to the terminology of Simpson (1989), is reached at $x \simeq 1.55$ m for all flow cases. Intermittent transitory detachment (ITD, $\gamma = 80\,\%$) occurs at $x \simeq 1.65$ m for the Medium and Large TSBs, but not for the Small TSB, where the minimum value of $\gamma$ on the centreline lies just over this threshold (81 %, see also figure 7). For the Medium and Large TSBs, the value $\gamma = 50\,\%$ that corresponds to the average detachment line (or transitory detachment, TD) is reached at $x \simeq 1.75$ m on the test-section centreline. This threshold in not reached in the case of the Small TSB. Thus, the Small TSB does not feature any region of mean back flow in a large portion of the test section and the flow can be considered to be attached in the mean. Moving downstream, the point of mean reattachment ($\gamma = 50\,\%$) is reached at $x = 1.90$ m for the Medium TSB and $x = 2.15$ m for the Large TSB. Finally, the positions where $\gamma = 99\,\%$ in the reattachment region, which can be dubbed 'complete reattachment' (CR), are reached further downstream ($x = 1.87$, $x = 2.07$, and $x = 2.27$ m for the Small, Medium and Large TSBs on the test-section centreline, respectively). Based on these measurements, the average separation length $L_b$, defined as the distance between mean detachment and mean reattachment on the test-section centreline is $L_b = 0.11$ m for the Medium TSB and $L_b = 0.40$ m for the Large TSB.

At this stage it is worth discussing the choice of length scale that should be used to compare the pressure and velocity distributions from different flow cases. The length $L_b$ is

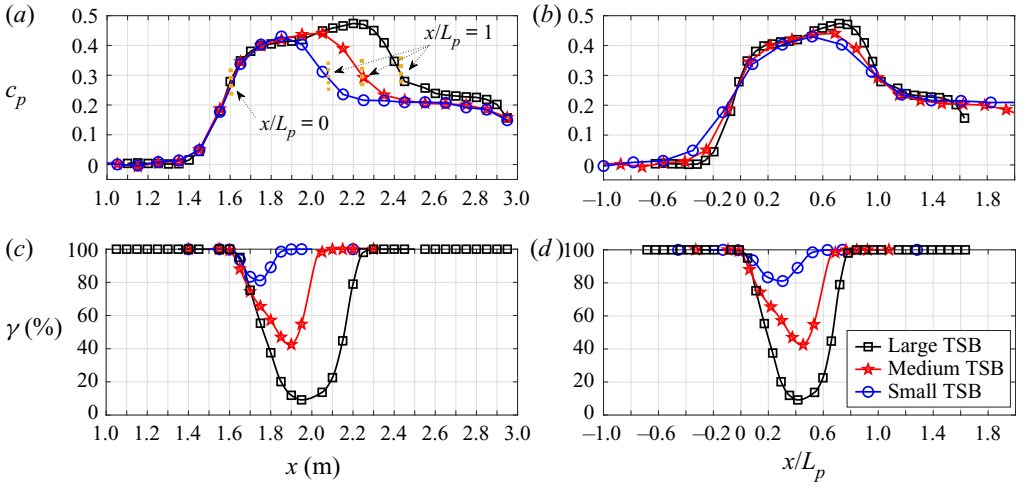


FIGURE 7. Distribution of pressure coefficient $c_p$ ($a$, $b$) and forward-flow fraction $\gamma$ ($c$,$d$). ($a$, $c$) Physical streamwise axis $x$; ($b$, $d$) streamwise distance scaled by $L_p$. The origin of $x/L_p$ is located at the streamwise position of maximum APG.

inappropriate because it is undefined when there is no region of mean back flow, as in the case of the Small TSB. Instead of $L_b$, Le Floc'h *et al.* (2017) suggested a length $L_{99}$ defined as the distance between the positions of incipient detachment and complete reattachment, where $\gamma = 99\,\%$. While more generally applicable, this definition requires the knowledge of the streamwise distribution of forward-flow fraction, which is not always available in existing references. For this reason we prefer to use a length $L_p$ similar to that introduced by Abe (2017) and defined as the distance between the positions of maximum APG and maximum FPG that are readily available in the published literature. The distributions of pressure coefficient $c_p$ and forward-flow fraction $\gamma$ on the test-section centreline are plotted as function of the physical streamwise distance $x$ and the normalized distance $x/L_p$ in figure 7. The advantage of the latter representation is that it reasonably collapses the distributions of $c_p$ and $\gamma$, which allows a comparison of different separation bubbles on the same axis system. Therefore, in the remainder of the article, comparison between different flow cases will be done using $x/L_p$.

Finally, a contour plot of the average longitudinal velocity fields, measured by PIV on the test-section centreline, is shown in figure 8. The difference in size between the three flow cases is obvious, with the Large TSB featuring an extensive region of mean back flow over a streamwise length of $x/L_p \simeq 0.5$, and the Medium TSB over a much smaller region $x/L_p \simeq 0.15$. These values of the separation length are consistent with those obtained with the calorimetric shear-stress sensor and plotted in figure 7. Note that the vertical extent of the back-flow region is approximately 26 mm for the Large TSB and 2.5 mm for the Medium TSB, resulting in vertical aspect ratios $H_b/L_b$ of 0.12 and 0.06, respectively, as documented in table 1.

### 3.2. *Pressure statistics*

A streamwise plot of the fluctuating pressure coefficient $c_{p'} = 2p_{rms}/\rho U_{ref}^2$, defined as the standard deviation of the fluctuating wall pressure normalized by the incoming dynamic pressure, is shown in figure 9 as a function of $x/L_p$. For the three flows the distribution is

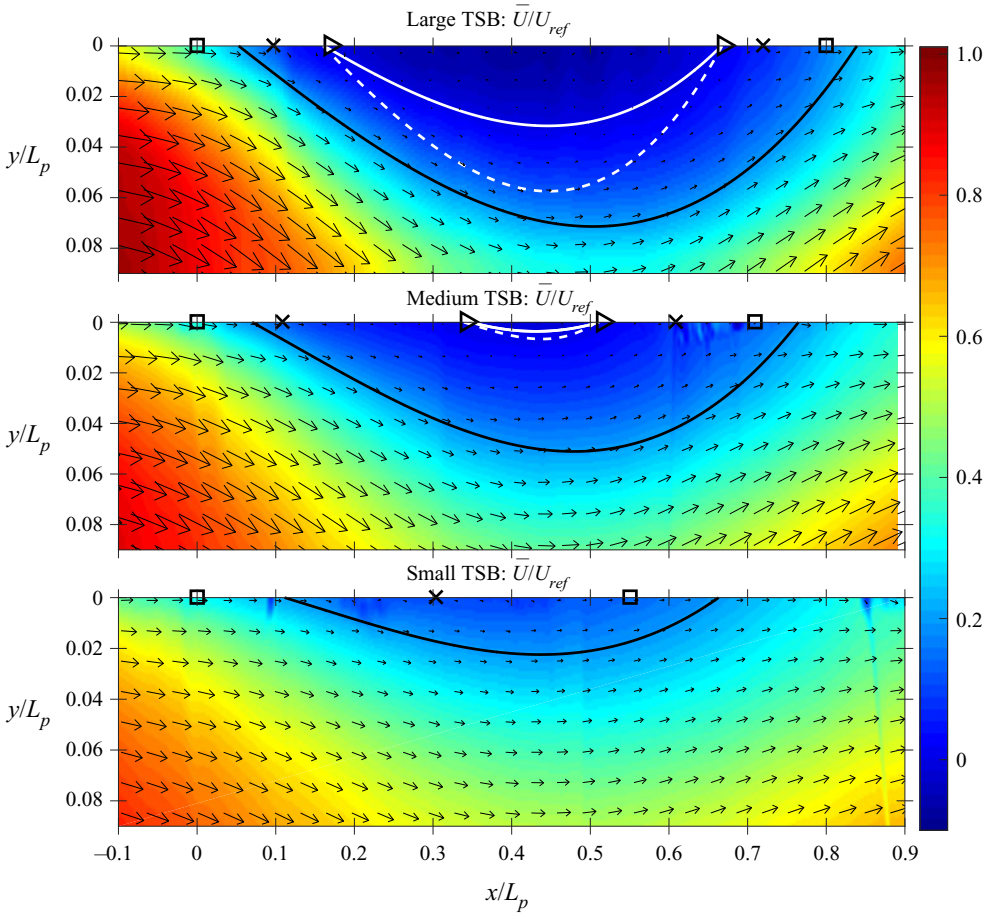


FIGURE 8. Average streamwise velocity contours for the three TSBs along the $x/L_p$ axis. Velocity vectors are superimposed. White solid lines are the isolines $\bar{U} = 0$ m s$^{-1}$, white dash lines are the mean dividing streamlines $\psi = 0$. Black lines are the isolines $\bar{U} = 5$ m s$^{-1}$. The black squares, crosses and triangles denote ID or CR ($\gamma = 99\,\%$), intermittent transitory detachment or reattachment ($\gamma = 80\,\%$) and transitory detachment or reattachment ($\gamma = 50\,\%$), respectively.

bi-modal, with a first maximum at $x/L_p \simeq 0$ and a second at $x/L_p \simeq 0.75$, though for the Small TSB this second maximum is almost non-existent. The pressure fluctuations clearly increase with the size of the TSB, especially near the second maximum at $x/L_p \simeq 0.75$. Coincidentally, for the Medium TSB both maxima have essentially the same value, whereas the second maximum is clearly larger than the first for the Large TSB, and respectively smaller for the Small TSB. A bi-modal distribution of $c_{p'}$ was also observed in the DNS of Na & Moin (1998*b*) and Abe (2017). The latter author investigated the influence of the TSB size on the wall-pressure fluctuations at $Re_\theta = 300$ and showed that consistently with the present results, fluctuations increase with the bubble size, particularly in the region of the second maximum. The large TSB in Abe (2017) has both maxima at approximately $c_{p'} = 0.20$, compared to $c_{p'} \simeq 0.12$ for our Medium TSB. At $Re_\theta = 900$ the second maximum for the large TSB in Abe (2017) remains at $c_{p'} \simeq 0.20$ whereas the first decreases to $c_{p'} \simeq 0.13$, thereby implying a significant Reynolds number effect. The first

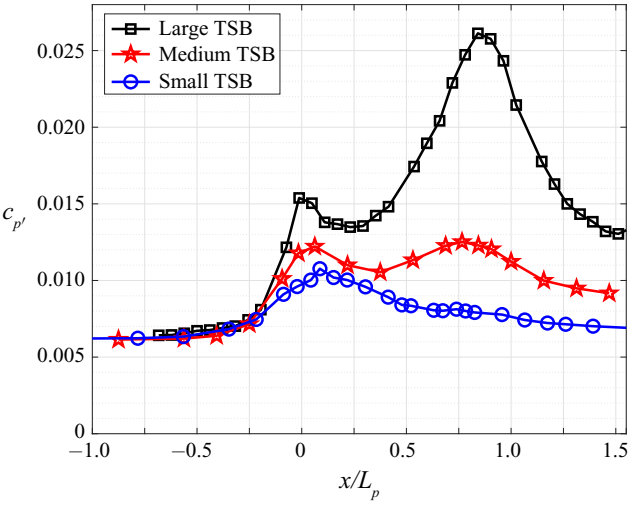


FIGURE 9. Fluctuating wall-pressure coefficient $c_{p'}$ measured on the test-section centreline for the three TSBs.

maximum in Na & Moin (1998*b*) is at $c_{p'} \simeq 0.13$ and their second maximum at $c_{p'} \simeq 0.18$, which corresponds to a distribution between our Medium and Large TSBs.

The wall-pressure fluctuations are investigated in the frequency domain in figure 10. The plot on the top of the figure shows the power spectral density (PSD) calculated at $x/L_p = 0$ and $x/L_p = 0.75$, i.e. the locations of the two maxima of figure 9, for the three separation bubbles. For reference, the PSD of pressure fluctuations in the incoming ZPG turbulent boundary layer is also provided. At $x/L_p = 0$, the PSD levels of the three TSBs are essentially the same for frequencies above 10 Hz. For $f < 10$ Hz, however, the amount of energy in the signals is larger for a larger bubble, consistently with the $c_{p'}$ distributions of figure 9. This shows that differences in the level of pressure fluctuations at $x/L_p \simeq 0$ are caused by low-frequency unsteady phenomena. Note also that the PSD levels in the three TSBs are higher than those of the incoming boundary layer in the complete frequency range that was investigated, which implies that even without the low-frequency contribution, a peak in $c_{p'}$ would be observed near $x/L_p = 0$. At $x/L_p = 0.75$, the shape of the PSDs is different. There is still an increase in energy with TSB size at low frequency ($f < 10$ Hz), however, the major difference occurs for frequencies between 10 Hz and 300 Hz, with the Large TSB again showing a stronger increase in energy compared to the others. For frequencies above 300 Hz the PSD levels decrease, even to values lower than in the ZPG boundary layer. These observations imply that the energy of the pressure fluctuations is essentially shifted from a broadband character in the incoming attached boundary layer to low ($f < 10$ Hz) and medium ($10 < f < 300$ Hz) frequencies under the separation bubbles, with the lower frequencies increasing earlier than the medium frequencies when moving in the streamwise direction.

Figure 10(*b*) shows the same data but plotted as the PSD pre-multiplied by the frequency and normalized by each signal's variance ($f \times PSD(f)/\sigma_{p'}^2$). This representation is useful because it shows the distribution of energy as the area under each curve in a semi-logarithmic plot since $\int_0^\infty PSD(f)\,\mathrm{d}f = \int_0^\infty f \times PSD(f)\,\mathrm{d}\ln(f)$. In this plot the low- and medium-frequency ranges are particularly obvious. At $x/L_p = 0$ the energy is concentrated in the low-frequency ($f < 10$ Hz) as well as the high-frequency ($f > 100$ Hz) range, with almost nothing in between. For the Large TSB there is almost the same

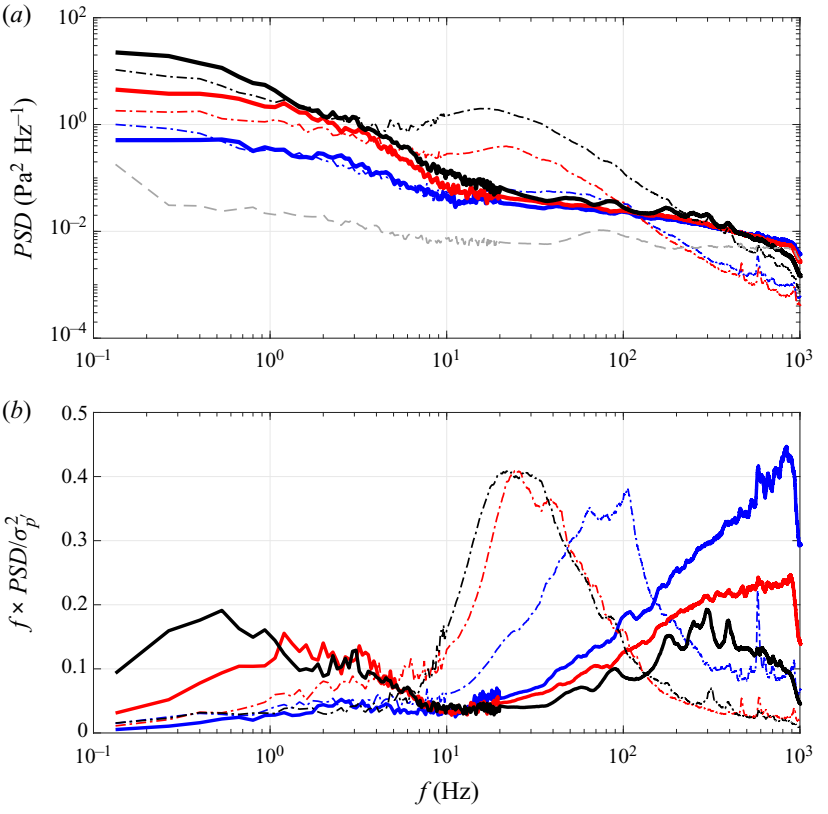


FIGURE 10. (*a*) Power spectral density of wall-pressure fluctuations at $x/L_p \simeq 0$ (solid lines) and $x/L_p \simeq 0.75$ (dash-dot lines). Black: Large TSB; red: Medium TSB; blue: Small TSB. Grey dashed line is the PSD measured in the incoming boundary layer upstream of separation ($x = 1.05$ m). (*b*) Pre-multiplied PSD normalized by the signal's variance, same colour coding as above.

amount of energy in the low-frequency as in the high-frequency range but for the Small and Medium TSBs, the high-frequency part is dominant. It is noteworthy that at $x/L_p = 0$, the pre-multiplied PSDs are cut-off by the anti-aliasing filter of the data acquisition card at $f \simeq 1$ kHz. This implies that the wall-pressure fluctuation levels are likely to be underestimated in the upstream part of our TSBs due to the limited temporal resolution of the pressure taps. Indeed, the review of Bull (1996) indicates an expected level of $c_{p'} = 0.009$ in our turbulent ZPG boundary layer at $Re_\theta = 5000$ (see his figure 1 with $u_\tau = 1$ m s$^{-1}$ and $\delta = 28$ mm), which is larger than $c_{p'} = 0.006$ obtained in the present experiment. This underestimation of $c_{p'}$, however, would only be limited to the incoming ZPG boundary layer and the very upstream part of our TSBs where the forward-flow fraction remains close to 100 % (see figure 7) and where the high-frequency pressure fluctuations are still significant (the effect of this limitation in our experimental technique will be further discussed in relationship with figure 15). In contrast to the spectra obtained a $x/L_p = 0$, those calculated at $x/L_p = 0.75$ show that almost all the energy of the fluctuating pressure is concentrated in a medium-frequency range, between $f \simeq 10$ Hz and $f \simeq 300$ Hz. The characteristic frequencies of these fluctuations, defined as the centre of the medium-frequency peak in the semi-logarithmic pre-multiplied representation, is

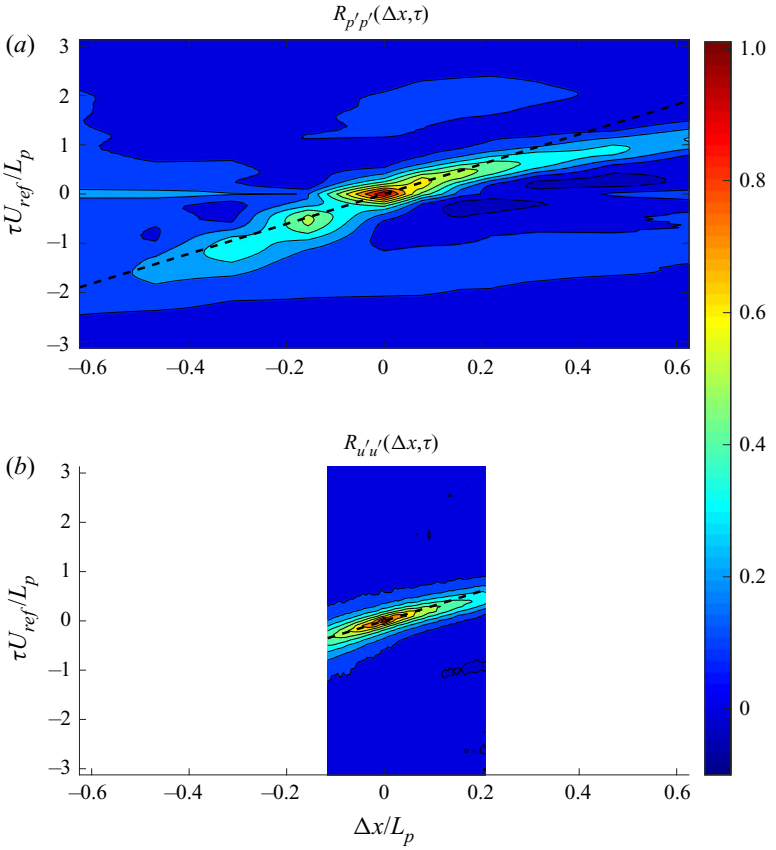


FIGURE 11. Contour of wall-pressure (*a*) and streamwise velocity (*b*) two-point cross-correlation along the test-section centreline (Medium TSB). The reference position is at $x_{ref} = 2.05$ m. The black dashed line is the slope corresponding to a convection velocity $U_c/U_{ref} = 0.33$ (Na & Moin 1998*b*).

approximately 25, 30 and 80 Hz for the Large, Medium and Small TSBs, respectively. The pre-multiplied PSDs further show than the frequency resolution of the measurements is more than adequate at these streamwise positions.

We now turn our attention to the mechanisms causing the low- and medium-frequency pressure fluctuations, beginning with the latter. In the case of the Large TSB, Mohammed-Taifour & Weiss (2016) showed that the pressure fluctuations near the second maximum of the $c_{p'}$ distribution in figure 9 are caused by the convection of large-scale, roller-type structures originating in the shear layer via a Kelvin–Helmholtz instability and subsequently shed downstream of the bubble. This medium-frequency unsteadiness was therefore called the 'shedding mode' of the TSB. To illustrate the convective nature of this unsteady mode, two-point cross-correlation contours of the wall-pressure and velocity fluctuations measured on the test-section centreline are presented in figure 11 for the case of the Medium TSB. The image on the top of the figure was obtained using a reference pressure transducer at a fixed position of $x_{ref}/L_p = 0.69$ (which corresponds to $x_{ref} = 2.05$ m), and a second pressure transducer covering the range $0.1 < x/L_p < 1.3$. On the bottom image, velocity cross-correlations were extracted from the PIV data along the centre of the shear layer defined by the loci of maximum $u'^2$, with again a reference

position at $x_{ref} = 2.05$ m. The streamwise extent of the cross-correlation plots is smaller for the velocity data because of the limited PIV field of view.

Both the pressure and velocity cross-correlation contours show a clear ridge indicating disturbances with a convective nature. The average slope of this ridge is a measure of the convection velocity of the large-scale structures, which is seen to be very close to the value of $U_c/U_{ref} = 0.33$ suggested by Na & Moin (1998*b*) and plotted as a dashed line in figure 11. The same analysis was performed on data from all three TSBs and essentially shows very similar results, including an almost constant value of the convection velocity. This is the case even for the Small TSB which does not feature any region of mean back flow. Thus, the occurrence of a convective shedding mode does not require the flow to reach an average separated state, but merely the presence of inflectional velocity profiles from the APG. This is consistent with the idea of coherent structures generated by Kelvin–Helmholtz instabilities in a manner similar to what is observed in turbulent mixing layers, as argued in Winant & Browand (1974). Nevertheless, a larger separation bubble clearly produces shedding with a larger pressure signature, as evidenced by figure 9. This is attributed to larger coherent structures when the shear layer separates further away from the wall.

In contrast to the convective medium-frequency shedding mode, the low-frequency unsteadiness in the Large TSB was shown to be linked to a large-scale contraction and expansion, dubbed 'breathing', of the whole separation bubble (Weiss *et al.* 2015). In particular, this breathing motion was well illustrated by the first proper orthogonal decomposition (POD) mode of the fluctuating velocity field (Mohammed-Taifour & Weiss 2016). The relevance of the first POD mode for studies of large-scale unsteadiness in TSBs was recently confirmed by Fang & Tachie (2019), who demonstrated that its time coefficient $a^1(t)$ is well synchronized with the time history of the total reverse-flow area $A_{xy}(t) = \iint_{x,y} -\mathrm{sign}(U(t))\,\mathrm{d}x\,\mathrm{d}y$. The latter indicator has been used by Pearson, Goulart & Ganapathisubramani (2013) and Wu *et al.* (2020) as a simple parameter that measures the large-scale unsteadiness in separation bubbles. $A_{xy}$ is most relevant for TSBs that feature large regions of instantaneous back flow at all time. This is the case in our Medium and Large TSBs, but not in our Small TSB. Therefore, in order to provide a more widely applicable indicator of large-scale unsteadiness, we introduce the quantity $B_{xy}(t) = \iint_{x,y}(U_{ref} - U(t))\,\mathrm{d}x\,\mathrm{d}y$, which essentially measures the instantaneous size of the decelerated flow region even in the absence of back flow. The time trace of $B_{xy}(t)$ is compared to the time coefficient $a^1(t)$ of the first POD mode of the longitudinal velocity field in figure 12. While these particular data were measured on the centreline plane of our Medium TSB, similar results were obtained for all three separation bubbles. The synchronization between the two signals is remarkable, which further consolidates the first POD mode as a relevant indicator of the breathing motion.

A snapshot POD analysis was performed on all three TSBs by using the PIV field of view closest to the centre of each bubble. The POD spectra showing the repartition of the longitudinal turbulent kinetic energy across the modes are shown in figure 13 for two sets of velocity data: the original (unfiltered) longitudinal velocity and the velocity digitally high-pass filtered at $f > 10$ Hz. Looking at the original velocity data first, it can be seen that the first POD mode is significantly more energetic than the second, with a difference of approximately 5 %, 10 % and 15 % between first and second POD modes for the Small, Medium and Large TSB, respectively. Since the first POD mode is representative of the breathing motion, this shows that the low-frequency breathing is more pronounced for a larger TSB, which is consistent with the Fourier analysis of figure 10 where the low-frequency pressure signature is clearly larger for a larger separation bubble.

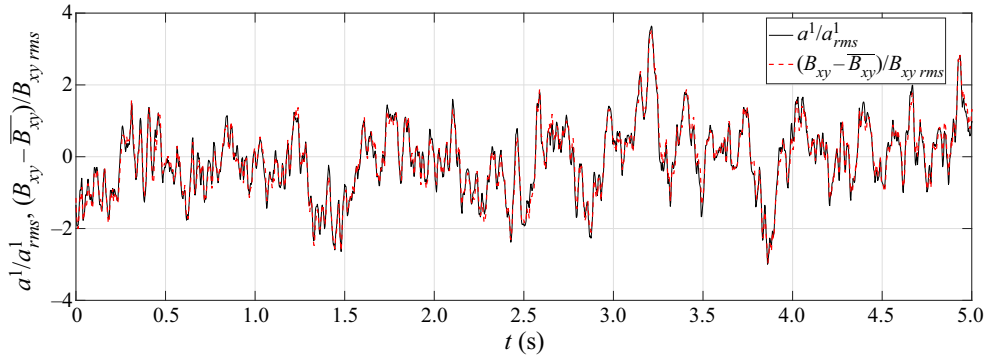


FIGURE 12. Time history of the first POD mode $a^1(t)$ and the decelerated-flow indicator $B_{xy}(t)$ on the test-section centreline, Medium TSB.

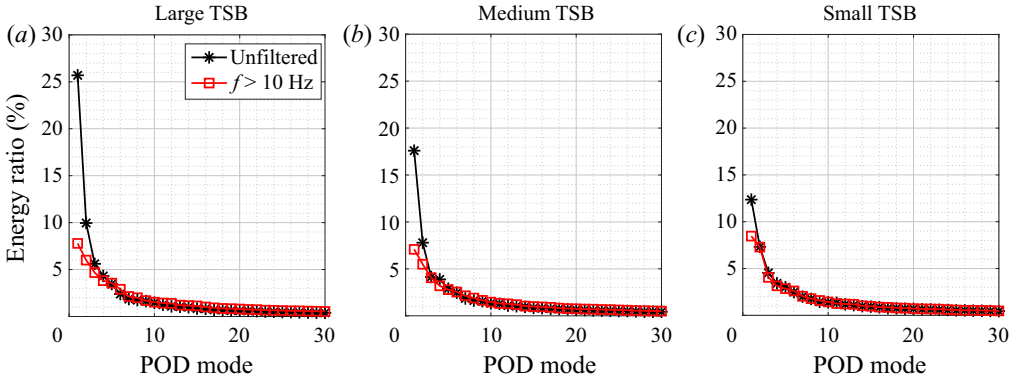


FIGURE 13. POD spectrum of longitudinal velocity fluctuations in the three TSBs (snapshot POD calculated from a field of view central to each separation bubble). Black stars: POD calculated on original velocity data. Red squares: POD calculated on data high-pass filtered at 10 Hz.

This analysis is confirmed by looking at the POD spectra obtained from the velocity fields high-pass filtered above 10 Hz: in this case there is only a few percentage points of difference between the first and second POD modes, irrespective of the size of the TSB. This confirms that for $f < 10$ Hz, the flow behaves somewhat differently than at higher frequencies.

The first three POD modes of the longitudinal velocity field in the Medium TSB are shown in figure 14, again for the original velocity field and the high-pass filtered field ($f > 10$ Hz). Note that similar results were obtained for all three separation bubbles. In the case of the original velocity, the first mode appears to be of uniform sign, and represents a contraction and expansion of the complete TSB since, when multiplied by its time coefficient $a^1(t)$, it exhibits a structure that effectively enlarges or shrinks the separation bubble (Mohammed-Taifour & Weiss 2016; Fang & Tachie 2019). In contrast, the subsequent modes show a change of sign, which is indicative of the convection of turbulent structures in the flow (Rajaee, Karlsson & Sirovich 1994; Weiss 2019). When only frequencies above 10 Hz are considered in the POD analysis, the uniform character of the first mode disappears and the convective nature of the fluctuations appears already in the first mode. Again, this is fully consistent with the spectral analysis of the pressure data

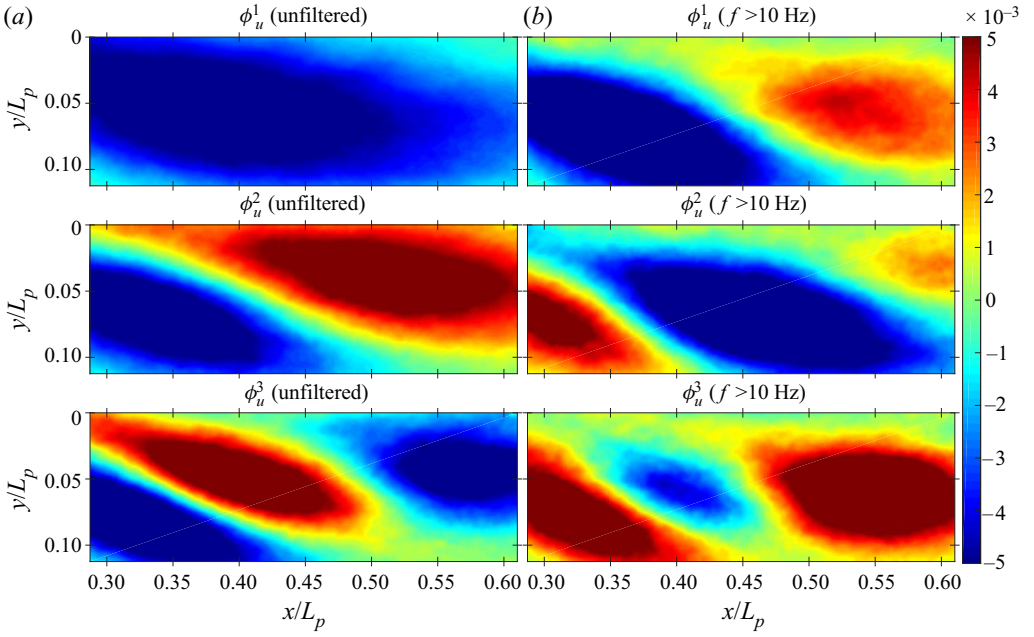


FIGURE 14. First, second and third POD modes of longitudinal velocity in the Medium TSB (arbitrary scale). (*a*) POD calculated on original velocity data. (*b*) POD calculated on data high-pass filtered at 10 Hz.

presented in figure 10 and confirms the presence of a low-frequency breathing mode for frequencies below 10 Hz, the intensity of which increases with the size of the TSB. This effect of TSB size is consistent with the recent DNS of Wu *et al.* (2020), who observed a much larger variation of the reverse-flow area $A_{xy}(t)$ for a large TSB generated with a suction-only boundary condition than for a smaller TSB obtained using suction and blowing.

Based on these new results, it would be of interest to plot the streamwise distribution of the fluctuating pressure coefficient for frequencies above 10 Hz only, as this would remove the pressure signature of the low-frequency breathing motion. This is done in figure 15, where the most interesting result is remarkably that the three curves now see their first maximum collapse on each other and exhibit approximately the same amplitude of $c_{p'} \simeq 0.01$ at $x/L_p = 0.1$. This streamwise position corresponds to the end of the strong adverse pressure-gradient zone and the beginning of the flow detachment from the wall, with approximately 10 % of reverse flow (figure 7). It also corresponds very well to the position of the first maximum of $c_{p'}$ observed in the direct simulations of Na & Moin (1998*b*) and Abe (2017). From the spectral plots of figure 10 it is obvious that at $x/L_p \simeq 0.1$, the pressure fluctuations are mostly confined to the low- and high-frequency parts of the spectrum. Removing the low-frequency breathing then implies that only the high-frequency turbulent motions are now taken into account. The rise in $c_{p'}$ up to $x/L_p = 0.1$ is then interpreted as the effect of the adverse pressure gradient on the turbulent structures responsible for pressure fluctuations in the attached boundary layer, while the decrease of $c_{p'}$ beyond $x/L_p = 0.1$ corresponds to the lifting of those structures away from the test surface in the early stages of detachment. This is consistent with the wall-normal profiles of pressure fluctuations shown by Na & Moin (1998*b*), as seen in

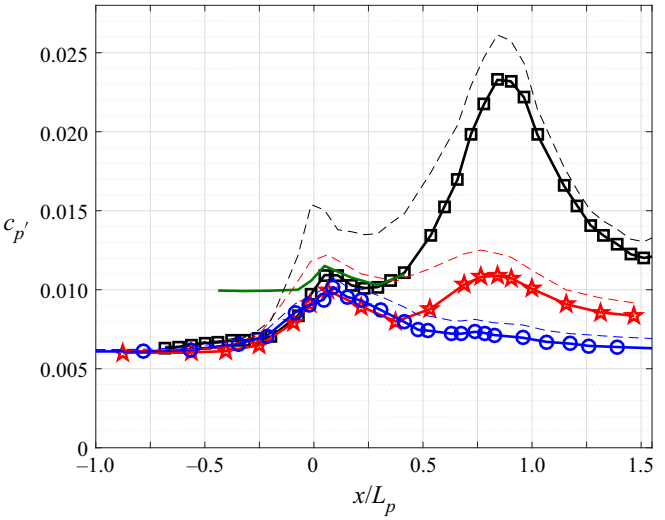


FIGURE 15. Fluctuating wall-pressure coefficient $c_{p'}$ measured on the test-section centreline for the three TSBs. Black: Large TSB, red: Medium TSB, blue: Small TSB. Dashed lines are unfiltered values from figure 9 while solid lines are high-pass filtered above 10 Hz. Solid green line are high-pass filtered data from flush-mounted pressure transducer ($f_s = 16$ kHz), Large TSB.

their figure 13, where the position of maximum pressure fluctuations is shown to move away from the wall at the very end of the pressure ramp. Furthermore, given that the APG imposed on the incoming turbulent boundary layer is essentially the same for all of our three TSBs (figure 1), it would be expected that the turbulent fluctuations react to the APG in approximately the same way upstream of the mean detachment. This is indeed confirmed by the filtered $c_{p'}$ distributions of figure 15.

A noteworthy feature that was previously mentioned in connection with figures 9 and 10 is the limited sampling frequency ($f_s = 2$ kHz) of the fluctuating wall-pressure measurements caused by the use of regular pressure taps instead of a frequency-calibrated pinhole. It was argued that the effect of this limited bandwidth would only be felt in the ZPG region and the most upstream part of the pressure-gradient zone. To investigate this in more details, dedicated measurements were performed in the Large TSB using a flush-mounted pressure transducer at a higher sampling frequency of $f_s = 16$ kHz. The results from figure 15 (green solid line) show that taking into account a larger frequency band increases $c_{p'}$ up to 0.010 in the ZPG region, which is very close to the value of 0.009 expected from the review of Bull (1996). The $c_{p'}$ level then slightly increases at $x/L_p \simeq 0.1$ and decreases afterwards, following the values obtained at a lower sampling frequency. This confirms that the wall-pressure measurement set-up is indeed adequate within the separation bubbles and demonstrates that the observation of a well-defined local maximum of $c_{p'}$ depends in fact on the selection of a specific frequency band.

In summary, the results presented in this section confirm the presence of a low-frequency unsteadiness whose amplitude appears to depend on the size of the TSB, with the largest pressure signature observed for the largest TSB. For the latter, Mohammed-Taifour & Weiss (2016) demonstrated that this unsteady character of pressure-induced separation bubbles was inherently linked to a contraction and expansion motion of the entire recirculation region. Removing this low-frequency contribution collapses the first maximum of the fluctuating pressure coefficient to a single value for all

three separation bubbles. Interestingly, the $c_{p'}$ distributions remain bi-modal after removal of the low-frequency contribution, which is consistent with the DNS results of Na & Moin (1998*b*) and Abe (2017), who did not resolve the low-frequency fluctuations. This shows that the first maximum of $c_{p'}$ is in fact the result of two separate phenomena: on the one hand, the signature of the low-frequency breathing motion, mostly apparent at the position of maximum adverse pressure gradient, and on the other hand the increase in high-frequency pressure fluctuations caused by the turbulent structures submitted to an APG and their subsequent lift-off from the wall. This reconciles the DNS results of Na & Moin (1998*b*) and Abe (2017) with the conclusions of Weiss *et al.* (2015) and Mohammed-Taifour & Weiss (2016) obtained from observations of the Large TSB only.

### 3.3. *Velocity statistics and scaling of pressure fluctuations*

In this section we investigate the velocity statistics obtained by PIV on the test-section centreline and the scaling of wall-pressure fluctuations with the Reynolds shear stresses and wall-normal stresses, as suggested by the previous works of Simpson *et al.* (1987), Na & Moin (1998*b*), Ji & Wang (2012) and Abe (2017).

Contour plots of the normalized turbulent streamwise $\overline{u'u'}/U_{ref}^2$, wall-normal $\overline{v'v'}/U_{ref}^2$ and shear $-\overline{u'v'}/U_{ref}^2$ stresses, are shown in figure 16. Note that the colour bars were adjusted to make the Small and Medium TSBs stand out more easily on the figure since the large bubble exhibits much higher values for all three Reynolds stresses. Therefore, the dark red areas in the third column are fully saturated. Nevertheless, the contours are consistent between the three separation bubbles and the amplitude of each turbulent stress generally increases with the size of the bubble. The loci of maximum stresses also tend to move away from the test surface as the TSB size grows. In the streamwise direction, $\overline{u'u'}/U_{ref}^2$ starts increasing slightly upstream of $x/L_p = 0$ and reaches its maximum near $x/L_p = 0.2$ (see also figure 17), which is consistent with the contours shown in Na & Moin (1998*a*) and those of Coleman *et al.* (2018); see figure 4 for a direct comparison between their case C and our Medium TSB. The wall-normal and shear stresses behave differently and increase from $x/L_p \simeq 0$ until the end of the PIV field of view. These contours are again close to those of Coleman *et al.* (2018), e.g. figure 4, but differ somewhat from those of Na & Moin (1998*a*) and Abe (2017), who observed a decrease of $\overline{v'v'}/U_{ref}^2$ and $-\overline{u'v'}/U_{ref}^2$ near the middle of their TSBs. This bi-modal distribution of the turbulent stresses is not observed in our data, except perhaps in the case of the Large TSB, where the Reynolds shear stress is seen to decrease slightly at $x/L_p \simeq 0.2$ compared to more upstream and downstream positions (see also figure 17). This aspect will be discussed further below.

The maxima of the three normalized turbulent stresses are plotted as a function of the streamwise position in figure 17. Given the relevance of the low-frequency contribution $f < 10\ Hz$ in the pressure fluctuations, the high-pass-filtered stresses are presented as well. It can be seen that removing the low-frequency contribution has the largest effect on the streamwise stresses, particularly near the middle of the TSB. The effects of filtering on the wall-normal and shear stresses are less significant and confined to the downstream part of the separation bubbles, where the stresses are themselves larger. For all stresses the largest difference between filtered and non-filtered data is seen on the Large TSB, which is consistent with the high-pass filtering of the pressure fluctuations (see figures 9 and 15). Note that high-pass filtering the velocity data enables a better comparison with existing DNS data, which, by current design, excludes low-frequency fluctuations. For example, the lowest Strouhal number resolved in the DNS of Abe (2017) is $St = fL_b/U_{ref} \simeq 0.13$, which corresponds to a dimensional frequency of approximately 8 Hz in our Large TSB. Regardless of the bandwidth taken into account, figure 17 shows a strong increase

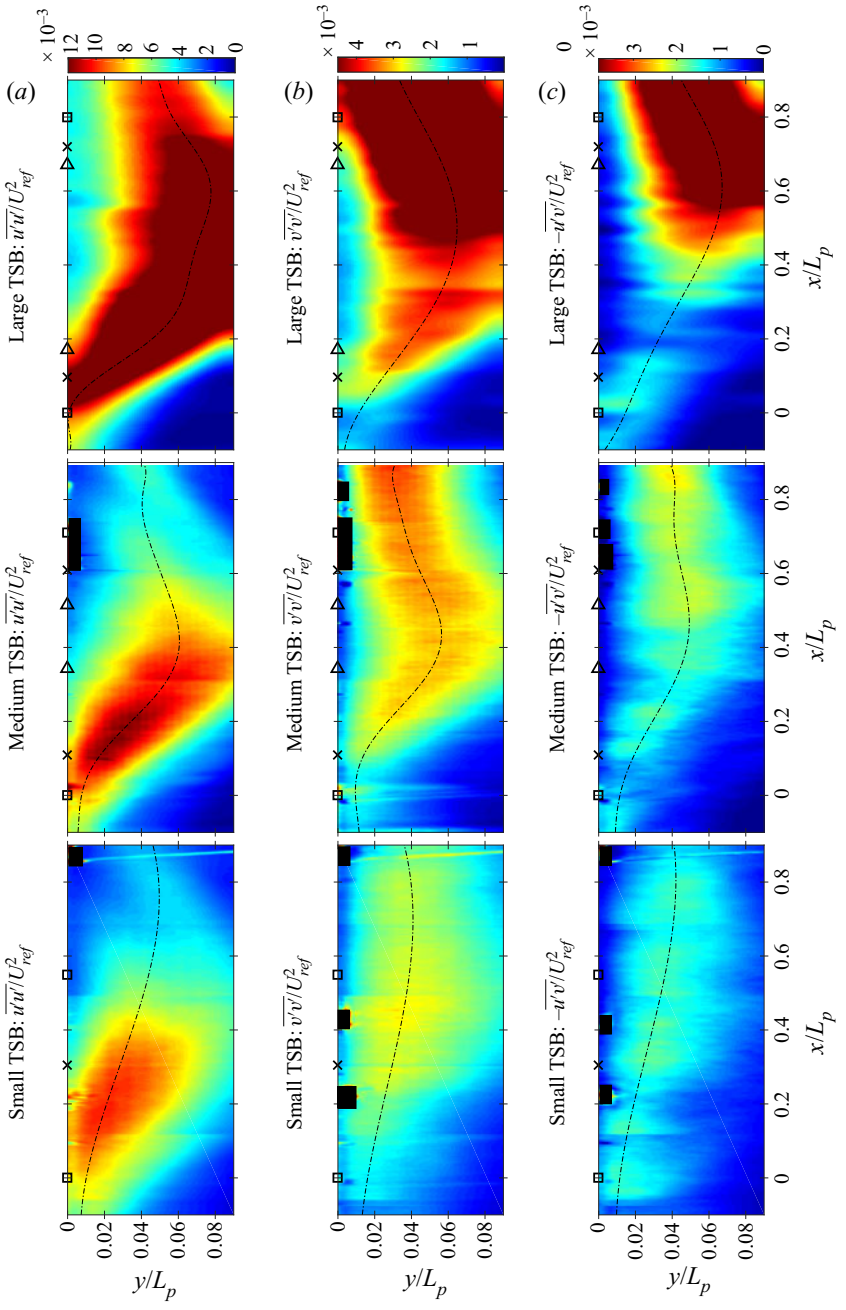


FIGURE 16. Contour plot of (*a*) $\overline{u'u'}/U_{ref}^2$, (*b*) $\overline{v'v'}/U_{ref}^2$ and (*c*) $-\overline{u'v'}/U_{ref}^2$ for the three TSBs. The black dash-dot lines are the loci of the maximum stresses. Black rectangles near the wall are caused by limitations in optical access. The black squares, crosses and triangles denote ID or CR ($\gamma = 99\,\%$), intermittent transitory detachment or reattachment ($\gamma = 80\,\%$) and transitory detachment or reattachment ($\gamma = 50\,\%$), respectively.

of $-\overline{u'v'}_{max}/U_{ref}^2$ and $\overline{v'v'}_{max}/U_{ref}^2$ in the reattachment region of the Large TSB, which is coincident with the large values of $c_{p'}$ in this region (figure 9). This indicates that the strong pressure signature of the shedding mode in the Large TSB is directly related to

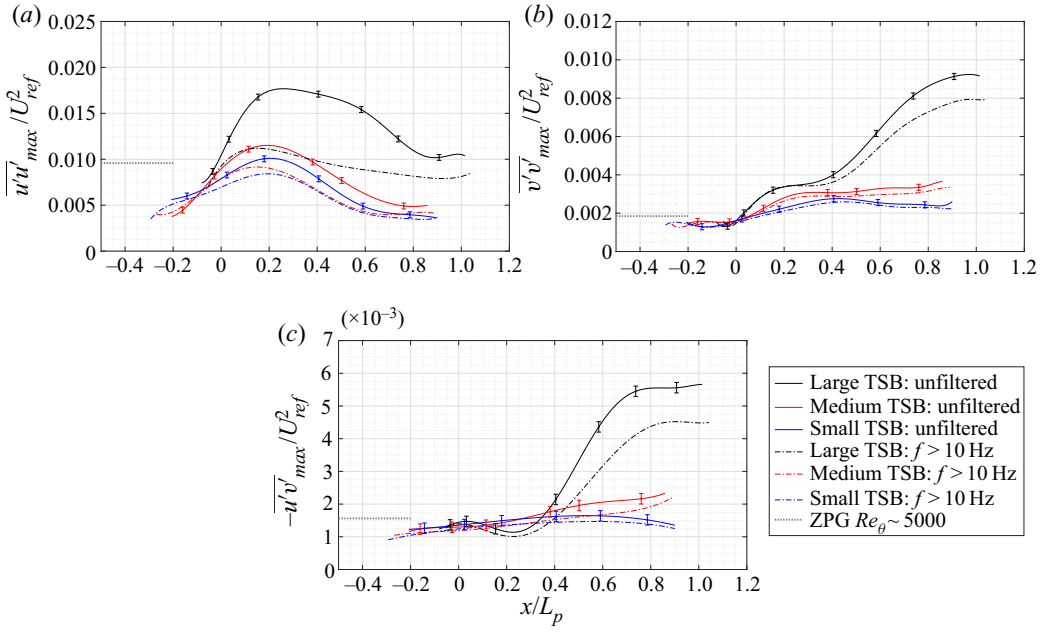


FIGURE 17. Maxima of (*a*) $\overline{u'u'}/U_{ref}^2$, (*b*) $\overline{v'v'}/U_{ref}^2$ and (*c*) $-\overline{u'v'}/U_{ref}^2$ for the three TSBs. Solid lines: original (unfiltered) data; dashed-dotted lines: data (high-pass) filtered at 10 Hz; black dotted lines are expected ZPG values from Fernholz & Finley (1996), for reference.

larger turbulent stresses, in agreement with the experimental results of Simpson *et al.* (1987) and the DNS of Na & Moin (1998*b*).

Also included in figure 17 are the values of the maximum turbulent stresses expected in a canonical ZPG turbulent boundary layer at $Re_\theta = 5000$, obtained from the review of Fernholz & Finley (1996). It can be seen that at the most upstream positions, our measured values are generally lower than the expected ZPG levels, with an underestimation of approximately 50 % for $\overline{u'u'}/U_{ref}^2$, 15 % for $\overline{v'v'}/U_{ref}^2$ and 20 % for $-\overline{u'v'}/U_{ref}^2$. This can be explained by the fact that at this Reynolds number, the wall-normal position of maximum stress is expected at 0.22, 5.4 and 2.9 mm for $\overline{u'u'}/U_{ref}^2$, $\overline{v'v'}/U_{ref}^2$ and $-\overline{u'v'}/U_{ref}^2$, respectively (Fernholz & Finley 1996). Given our spatial resolution of 0.55 mm and the inherent limitations of PIV measurements very near the wall, this difference is not surprising. Nevertheless, this underestimation should only be significant in the most upstream part of the TSBs (see the favourable comparison between hot-wire and PIV measurements of $\overline{u'u'}/U_{ref}^2$ in Mohammed-Taifour & Weiss (2016) for the case of the Large TSB).

In analysing figure 17, it is of interest to compare with the results of Abe (2017), who also investigated the effect of varying the TSB size on the streamwise distributions of $-\overline{u'v'}_{max}/U_{ref}^2$ and $\overline{v'v'}_{max}/U_{ref}^2$. This was done by varying the maximum transpiration velocity $[V_{top}/U_{ref}]_{max}$ at a constant Reynolds number $Re_\theta = 300$. Consistently with our data, both $-\overline{u'v'}_{max}/U_{ref}^2$ and $\overline{v'v'}_{max}/U_{ref}^2$ were shown to increase with the size of the bubble near the reattachment. The increase was more moderate closer to the detachment, however, and $-\overline{u'v'}_{max}/U_{ref}^2$ even decreased near the middle of the TSB when the bubble got larger. This was attributed, according to Abe, to a negative TKE production rate near the top of the bubble that arises because of the rapid switch between positive and negative

vertical transpiration velocity. As $[V_{top}/U_{ref}]_{max}$ is increased to generate a larger TSB, the production term becomes more negative and $-\overline{u'v'}_{max}/U_{ref}^2$ decreases (Abe 2017). This argument is consistent with the small decrease of $-\overline{u'v'}_{max}/U_{ref}^2$ that is observed near $x/L_p = 0.2$ for our Large TSB only.

Further comparisons between our experimental data (Medium and Large TSB) and the distributions of $-\overline{u'v'}_{max}/U_{ref}^2$ and $\overline{v'v'}_{max}/U_{ref}^2$ from other sources are presented in figure 18. Starting with $-\overline{u'v'}_{max}/U_{ref}^2$, it can be seen that our Medium TSB and the Coleman *et al.* (2018) case C stand out by showing a monotonic increase with $x/L_p$. All other distributions, including CRS case A, show a clear minimum between $x/L_p = 0.3$ and $x/L_p = 0.7$. As already discussed above, this minimum is attributed to the larger value of $[V_{top}/U_{ref}]_{max}$ for large separation bubbles, which leads to smaller TKE production rate when $[V_{top}/U_{ref}](x)$ crosses zero and hence to a decrease of $-\overline{u'v'}/U_{ref}^2$ below the top of the bubble (Abe 2017; Coleman *et al.* 2018). For our Large TSB the value of $[V_{top}/U_{ref}]_{max}$ is large enough to show a small dip in $-\overline{u'v'}_{max}/U_{ref}^2$ near $x/L_p = 0.2$, in a manner very similar to the Patrick (1987) data. The values of $-\overline{u'v'}_{max}/U_{ref}^2$ obtained by Na & Moin (1998*a*), Abe (2017) (cases SB2 and LB) and Coleman *et al.* (2018) (case A) for $x/L_p < 0.5$ are relatively large compared to our data, to the Coleman *et al.* (2018) case C and to Patrick (1987). This is attributed to a lower Reynolds number for those former cases. Indeed, the results of Abe (2017) clearly indicate a decrease of $-\overline{u'v'}_{max}/U_{ref}^2$ (and to a lesser extent $\overline{v'v'}_{max}/U_{ref}^2$) when the Reynolds number increases, which is consistent with figure 18. The combined effects of a larger $[V_{top}/U_{ref}]_{max}$ and a larger Reynolds number, which have opposite effects on the value of $-\overline{u'v'}_{max}/U_{ref}^2$ for $x/L_p < 0.5$, may also explain why the Patrick (1987) data are very close to our Large TSB. Moving on to the downstream half of the bubbles ($x/L_p > 0.5$) indicates that $-(\overline{u'v'})_{max}$ essentially increases with the size of the TSBs and, consistently with the values of $H_b/L_b$ shown in table 1, the Patrick (1987) data show the largest value of $-\overline{u'v'}_{max}/U_{ref}^2$ near reattachment.

The distributions of $\overline{v'v'}_{max}/U_{ref}^2$ (bottom of figure 18) are generally consistent with those of $-\overline{u'v'}_{max}/U_{ref}^2$ in as much as a larger TSB generates a larger stress in the downstream half of the bubble. The results of Abe (2017) (cases SB2 and LB) and Coleman *et al.* (2018) (case A) show a bi-modal distribution with a minimum of $\overline{v'v'}_{max}/U_{ref}^2$ near $x/L_p = 0.5 - 0.6$, while the others show a monotonic increase with a plateau near $x/L_p = 0.3$ (note that Na & Moin (1998*a*) did not publish their distribution of $\overline{v'v'}_{max}/U_{ref}^2$). This difference is attributed to the combined effect of Reynolds number and TSB size, where a larger Reynolds number tends to bring the first peak down, and a larger TSB the second peak up. Note that for a large bubble, the streamwise increase of $\overline{v'v'}/U_{ref}^2$ tends to start more upstream than $-\overline{u'v'}/U_{ref}^2$ (see figure 16), which explains the large value of $\overline{v'v'}_{max}/U_{ref}^2$ downstream of $x/L_p = 0.2$ for the Patrick (1987) fairly large TSB.

The scaling of the wall-pressure fluctuations with the maximum Reynolds shear stresses $-\rho\overline{u'v'}_{max}$ and the wall-normal stresses $\rho\overline{v'v'}_{max}$ is presented in figure 19. The high-pass filtered results are used for our data, which collapses the values of $p_{w\ rms}$ near $x/L_p = 0$ by removing the effect of the low-frequency breathing motion. As already mentioned above, this enables a more rigorous comparison with existing DNS data. Also, the expected ZPG levels obtained using the wall-pressure data collected by Bull (1996) and the turbulence data reviewed by Fernholz & Finley (1996) are included in the figure. The measured distributions of $p_{w\ rms}/-\rho\overline{u'v'}_{max}$ and $p_{w\ rms}/\rho\overline{v'v'}_{max}$ are seen to converge towards these

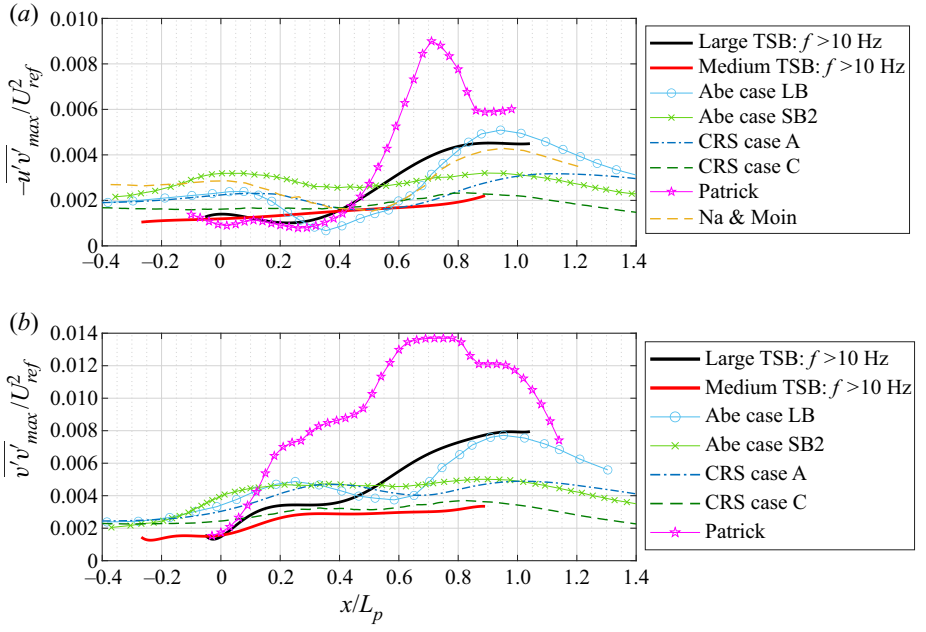


FIGURE 18. Maxima of $-\overline{u'v'}/U_{ref}^2$ (*a*) and $\overline{v'v'}/U_{ref}^2$ (*b*) for current and existing TSB data. Current data high-pass filtered at 10 Hz.

levels, which gives confidence in the results despite the experimental limitations observed in the most upstream part of the TSBs.

In a separating turbulent boundary layer, Simpson *et al.* (1987) experimentally found that $p_{w\ rms}/-\rho\overline{u'v'}_{max}$ increases up to a value of approximately 4 near the detachment and decreases afterwards. This is consistent with the behaviour obtained in the present experiment, though our Large TSB shows a larger maximum value of $p_{w\ rms}/-\rho\overline{u'v'}_{max} = 5$ near $x/L_p = 0.2$. The Na & Moin (1998*b*) and Abe (2017) data show essentially the same trend, but with slightly lower values. Generally speaking, both scalings succeed very well in collapsing the large differences in $c_{p'}$ observed near reattachment for the three TSBs (figure 15), though the scaling with $\rho\overline{v'v'}_{max}$ is perhaps better over a longer distance. Nevertheless, neither scaling law is fully satisfactory over the full length of the separation bubbles since the value of $p_{w\ rms}/-\rho\overline{u'v'}_{max}$ and $p_{w\ rms}/\rho\overline{v'v'}_{max}$ is not constant over $x$. This indicates that the mechanisms leading to wall-pressure fluctuations are not identical near the detachment and near the reattachment, which is consistent with the spectral analysis of figure 10 showing a separation of scales into low-frequency breathing, medium-frequency shedding and high-frequency turbulent fluctuations. Note also that using unfiltered data would reduce the quality of both scalings by increasing the discrepancies between the three TSBs at $x/L_p \simeq 0$ (Le Floc'h *et al.* 2019). This indicates that the low-frequency breathing motion does not appear to be directly related to turbulent stresses.

### 3.4. *Three-dimensional effects*

In this last section we take a look at the pressure fluctuations and their scaling across the span of the wind tunnel, as the discussion in § 3.1 revealed the presence of secondary flows affecting a large portion of the test section.

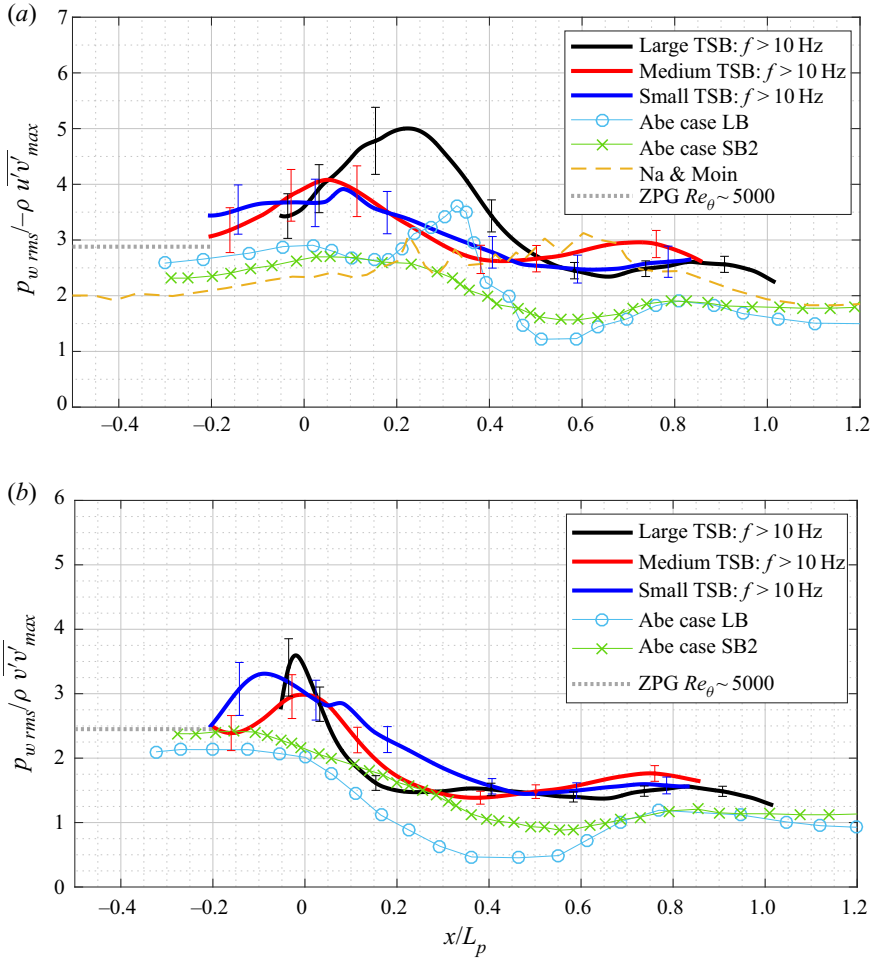


FIGURE 19. Scaling of wall-pressure fluctuations with $-\rho\overline{u'v'}_{max}$ (*a*) and $\rho\overline{v'v'}_{max}$ (*b*). Current data high-pass filtered at 10 Hz. Error bars were computed by propagating the uncertainties quantified in § 2.2.

The spanwise variation of the fluctuating pressure coefficient $c_{p'}$ is presented in figure 20 for the three separation bubbles. Apart from small imperfections, all curves are essentially symmetric with respect to the test-section centreline, but show significant variations of amplitude across the span. The spanwise effects appear to be stronger near reattachment ($x/L_p = 1$) than near detachment ($x/L_p = 0$), which is consistent with the global character of the average flows: as illustrated by the RANS results of figure 6, the corner vortices generated by secondary flows on the sidewalls slowly increase in size as the flow develops downstream of the mean separation, which implies a larger spanwise 'contamination' as the flow proceeds towards the exit of the test section (Le Floc'h *et al.* 2018). Furthermore, the three-dimensional effects appear to be strongest for the Medium TSB since at $x/L_p \simeq 1$, $c_{p'}$ is only approximately constant in a narrow region near the test-section centreline ($|z^*| < 1/6$). For the Small and Large TSBs, the quasi-two-dimensional extent of the flow is somewhat larger, with pressure fluctuations that are essentially constant over a third of the span ($|z^*| < 1/3$). Interestingly, the spanwise extent of the quasi-two-dimensional

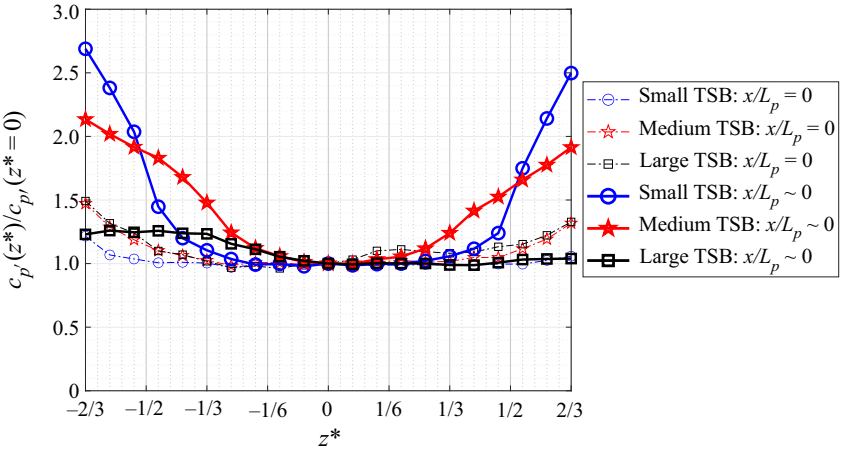


FIGURE 20. Normalized fluctuating pressure coefficient measured across the test section's span.

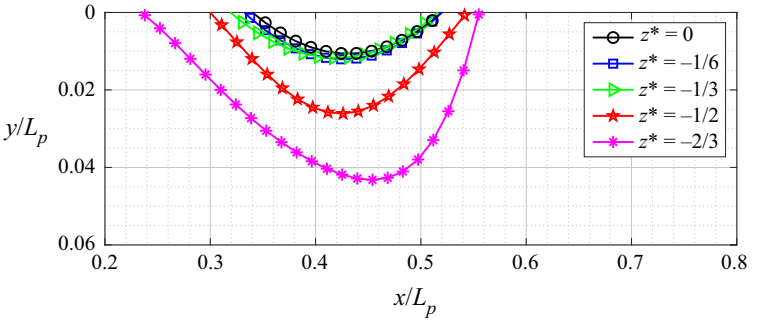


FIGURE 21. Mean dividing streamline ($\psi = 0$) for different spanwise positions, Medium TSB.

regions revealed by the pressure fluctuations is slightly smaller than that observed in the oil-film visualizations of figure 5. Defining the width $w_{2D}$ as the approximate extent of the quasi-two-dimensional flow observed from figure 20, the values of $w_{2D}/L_p$ are 0.43, 0.16 and 0.24 for the Small, Medium and Large TSBs, respectively. As can be seen in table 1, this is smaller than the spanwise extent of most existing numerical simulations.

In order to investigate three-dimensional effects in more details, further PIV measurements were performed in the Medium TSB. The field of view was limited to $0.2 < x/L_p < 0.6$ but the cameras were translated in the spanwise direction in order to image the separation bubble at 5 positions across the span of the test section. Measurements were only taken on one side of the test section, given the appropriate symmetry of the oil-film visualizations in figure 5 and of the pressure fluctuations in figure 20. The height of the local recirculation regions, identified by the mean dividing streamline $\psi = 0$ calculated at each spanwise position, is shown in figure 21. It can be seen that the separation bubble is strongly distorted across the span, with a larger bubble height near the sidewall than near the centreline. This distortion is caused by the corner vortices discussed in § 3.1. Near the sidewalls, the larger recirculation region increases the wall-pressure and the corresponding velocity fluctuations in a manner consistent with the increase of fluctuations with TSB size, as described in §§ 3.2 and 3.3.

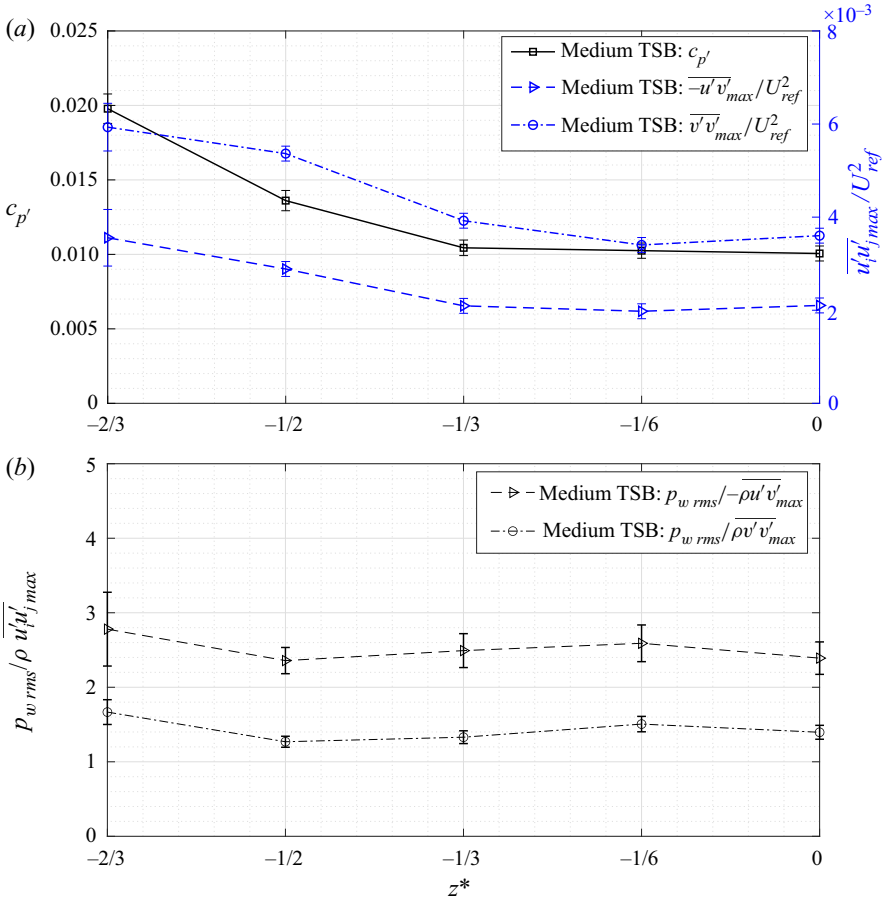


FIGURE 22. (*a*) Spanwise distributions of $c_{p'}$, $-\overline{u'v'}_{max}/U_{ref}^2$ and $\overline{v'v'}_{max}/U_{ref}^2$. (*b*) Spanwise distributions of $p_{w\,rms}/-\rho\overline{u'v'}_{max}$ and $p_{w\,rms}/\rho\overline{v'v'}_{max}$. Medium TSB at $x/L_p = 0.45$.

Nevertheless, the scaling of wall-pressure fluctuations proposed above appears to hold in the spanwise direction. Figure 22 shows the spanwise variation of $c_{p'}$, $-\overline{u'v'}_{max}/U_{ref}^2$ and $\overline{v'v'}_{max}/U_{ref}^2$ at $x/L_p = 0.45$. Both turbulent stresses display a similar trend as the pressure fluctuations, which leads to a nearly constant value of $p_{w\,rms}/-\rho\overline{u'v'}_{max}$ and $p_{w\,rms}/\rho\overline{v'v'}_{max}$ across the span. We conclude that although corner effects strongly distort the average flow, the unsteady character of the TSBs and the scaling of the pressure fluctuations remain relatively unaffected. While the spanwise PIV measurements were only performed on the Medium TSB, where three-dimensional effects are the strongest, it is reasonable to expect a similar behaviour for the small and large separation bubbles as well. Therefore, although the separation bubbles generated in our wind tunnel are necessarily unique in as much as they depend on the test-section geometry, the flow physics investigated in this work appears to be of general nature.

## 4. Conclusion

The main objective of the present study was to document wall-pressure and velocity fluctuations in a family of three incompressible, pressure-induced, turbulent separation

bubbles of various sizes, with a particular emphasis on the energetic low and medium frequencies. The three TSBs were generated by imposing specific pressure distributions on a ZPG boundary layer at $Re_\theta \simeq 5000$. The two largest separation bubbles feature a region of mean back flow but the smallest does not. The corresponding distributions of average pressure coefficient and vertical velocity in the potential flow were compared to those published by other authors. The flow near the centreline of our Medium TSB is fairly close to the case C investigated by Coleman *et al.* (2018) via DNS.

In all three cases, the streamwise distribution of wall-pressure fluctuations features two maxima, the first close to the position of maximum adverse pressure gradient ($x/L_p = 0$) and the second at the end of the region of intermittent back flow ($x/L_p \simeq 0.75$). The first (upstream) maximum was shown to be caused by the superposition of two separate phenomena occurring at approximately the same streamwise position: first, the signature of a low-frequency contraction and expansion (breathing) of the complete separation bubble, mostly noticeable at the position of maximum adverse pressure gradient, and documented by Mohammed-Taifour & Weiss (2016) in the case of the Large TSB. The amplitude of this low-frequency breathing was further shown to increase with the size of the separation bubble. The other phenomenon leading to the first streamwise peak in $c_{p'}$ is the effect of the adverse pressure gradient on the turbulent structures responsible for pressure fluctuations in the attached boundary layer, which reaches a maximum just before the flow lifts off from the wall. The amplitude of this effect is constant for the three TSBs because in our particular experimental set-up, the size of the separation bubble is changed by modifying the position of the FPG but not the APG. These findings reconcile the DNS results of Na & Moin (1998*b*) and Abe (2017) with the conclusions of Weiss *et al.* (2015) and Mohammed-Taifour & Weiss (2016) in that both the high-frequency turbulent fluctuations and the low-frequency breathing motion are jointly responsible for the first streamwise peak of $c_{p'}$ in pressure-induced TSBs.

The second (downstream) maximum of the $c_{p'}$ distribution occurs because of the impingement of large-scale, roller-type turbulent structures on the wall. These structures originate in the shear layer through a Kelvin–Helmholtz-type instability and are convected around the recirculation region. Here also, the pressure signature of this convective shedding mode strongly increases with the size of the separation bubble. Spectral analysis indicates that the energy of the wall-pressure fluctuations is shifted from a broadband character in the incoming ZPG boundary layer to low (0–10 Hz) and medium (10–300 Hz) frequencies under the separation bubbles. The low and medium frequencies correspond to the breathing and shedding mechanisms, respectively.

Distributions of the turbulent streamwise $\rho\overline{u'u'}_{max}$, wall-normal $\rho\overline{v'v'}_{max}$ and shear $-\rho\overline{u'v'}_{max}$ stresses were measured and compared to the existing literature values. In contrast to most numerical results, where the turbulent stresses have a bi-modal character similar to the wall-pressure fluctuations, both the wall-normal and shear stresses show a monotonic increase with the streamwise distance. This difference is a consequence of the higher Reynolds number and weaker transpiration profile of our TSBs compared to most existing numerical simulations. The only exception is the Coleman *et al.* (2018) case C, which has a similar transpiration profile as in our flows and a reasonably high Reynolds number, and which matches well our distribution of turbulent stresses. The scaling of the wall-pressure root mean square with both the Reynolds shear stress and the wall-normal stress was shown to be reasonably close to the DNS results of Na & Moin (1998*b*) and Abe (2017), which were the only available data sets so far. In particular, the scaling $p_{w\ rms}/\rho\overline{v'v'}_{max}$ is very successful in removing the large differences in pressure fluctuations in the second half of the separation bubbles. Near detachment, the removal of

the low-frequency contribution caused by the breathing of the bubbles provides a better scaling.

Finally, a detailed investigation of the three-dimensional nature of the average flow in the rectangular wind-tunnel test section, helped by a qualitative RANS simulation of the medium-sized TSB, showed that corner effects strongly distort the average separation bubbles and can lead to larger wall-pressure and velocity fluctuations near the side walls. Nevertheless, the scaling laws measured on the test-section centreline appear to hold reasonably well across at least two thirds of the test-section span.

These experimental results provide new insights into the unsteady character of pressure-induced turbulent separation bubbles, notably by isolating the effects of the low-frequency contraction and expansion (breathing) in the measurement of pressure and velocity fluctuations. This being said, the mechanism responsible for this breathing motion remains to be clarified.

## Acknowledgements

This work was supported by the Fonds de Recherche du Québec – Natures et technologies, the Natural Sciences and Engineering Research Council of Canada and the Canadian Foundation for Innovation. The authors acknowledge the support of E. Jondeau during the PIV experiments and thank Dr G. Coleman for providing access to the DNS database of CRS 2018.

## Declaration of interests

The authors report no conflict of interest.

## REFERENCES

ABE, H. 2017 Reynolds-number dependence of wall-pressure fluctuations in a pressure-induced turbulent separation bubble. *J. Fluid Mech.* **833**, 563–598.

ALVING, A. E. & FERNHOLZ, H. H. 1996 Turbulence measurements around a mild separation bubble and downstream of reattachment. *J. Fluid Mech.* **322**, 297–328.

ANGELE, K. P. & MUHAMMAD-KLINGMANN, B. 2006 PIV measurements in a weakly separating and reattaching turbulent boundary layer. *Eur. J. Mech.* B/*Fluids* **25** (2), 204–222.

BENDAT, J. S. & PIERSOL, A. G. 2010 *Random Data: Analysis and Measurement Procedures*, 3rd edn. John Wiley & Sons.

BOURIGA, M., TAHER, R., MORENCY, F. & WEISS, J. 2015 Numerical investigation of secondary flows in a constant-width wind-tunnel contraction. *Aeronaut. J.* **119** (1215), 613–630.

BRADSHAW, P. 1987 Turbulent secondary flows. *Annu. Rev. Fluid Mech.* **19** (1), 53–74.

BUICE, C. U. 1997 Experimental investigation of flow through an asymmetric plane diffuser. PhD thesis, Stanford University.

BUICE, C. U. & EATON, J. K. 1995 Experimental investigation of flow through an asymmetric plane diffuser. In *CTR Annu. Res. Briefs 1995*, pp. 117–120. Center for Turbulence Research.

BULL, M. K. 1996 Wall-pressure fluctuations beneath turbulent boundary layers: some reflections on forty years of research. *J. Sound Vib.* **190** (3), 299–315.

CHENG, W., PULLIN, D. I. & SAMTANEY, R. 2015 Large-eddy simulation of separation and reattachment of a flat plate turbulent boundary layer. *J. Fluid Mech.* **785**, 78–108.

CIAMPOLI, F. & HANCOCK, P. E. 2006 Effects of flow width in nominally two-dimensional turbulent separated flows. *Exp. Fluids* **40** (2), 196–202.

COLEMAN, G. N., RUMSEY, C. L. & SPALART, P. R. 2018 Numerical study of turbulent separation bubbles with varying pressure gradient and Reynolds number. *J. Fluid Mech.* **847**, 28–70.

DELERY, J. M. 1985 Shock wave/turbulent boundary layer interaction and its control. *Prog. Aerosp. Sci.* **22** (4), 209–280.

DENGEL, P. & FERNHOLZ, H. H. 1990 An experimental investigation of an incompressible turbulent boundary layer in the vicinity of separation. *J. Fluid Mech.* **212**, 615–636.

DIANAT, M. & CASTRO, I. P. 1989 Measurements in separating boundary layers. *AIAA J.* **27** (6), 719–724.

DIANAT, M. & CASTRO, I. P. 1991 Turbulence in a separated boundary layer. *J. Fluid Mech.* **226**, 91–123.

DRIVER, D. 1991 Reynolds shear stress measurements in a separated boundary layer flow. *AIAA Paper* 1991-1787.

FANG, X. & TACHIE, M. F. 2019 On the unsteady characteristics of turbulent separations over a forward–backward-facing step. *J. Fluid Mech.* **863**, 994–1030.

FERNHOLZ, H. H. & FINLEY, P. J. 1996 The incompressible zero-pressure-gradient turbulent boundary layer: an assessment of the data. *Prog. Aerosp. Sci.* **32** (4), 245–311.

JI, M. & WANG, M. 2012 Surface pressure fluctuations on steps immersed in turbulent boundary layers. *J. Fluid Mech.* **712**, 471–504.

KALTENBACH, H.-J., FATICA, M., MITTAL, R., LUND, T. S. & MOIN, P. 1999 Study of flow in a planar asymmetric diffuser using large-eddy simulation. *J. Fluid Mech.* **390**, 151–185.

LE FLOC'H, A., MOHAMMED-TAIFOUR, A., DUFRESNE, L. & WEISS, J. 2018 Spanwise aspects of unsteadiness in a pressure-induced turbulent separation bubble. *AIAA Paper* 2018-3538.

LE FLOC'H, A., MOHAMMED-TAIFOUR, A., DUFRESNE, L. & WEISS, J. 2019 Investigation of wall-pressure fluctuations in three pressure-induced turbulent separation bubbles. *AIAA Paper* 2019-3650.

LE FLOC'H, A., MOHAMMED-TAIFOUR, A. & WEISS, J. 2017 Investigation of the low-frequency breathing motion in two turbulent separation bubbles. *AIAA Paper* 2017-3970.

MA, A., GIBEAU, B. & GHAEMI, S. 2020 Time-resolved topology of turbulent boundary layer separation over the trailing edge of an airfoil. *J. Fluid Mech.* **891**, A1.

MENTER, F. R., GARBARUK, A. V. & EGOROV, Y. 2012 Explicit algebraic Reynolds stress models for anisotropic wall-bounded flows. *Prog. Flight Phys.* **3**, 89–104.

MOHAMMED-TAIFOUR, A., DUFRESNE, L. & WEISS, J. 2019 Numerical simulation of a large pressure-induced turbulent separation bubble. In *Proceedings of the 27th Canadian Congress of Applied Mechanics*. Université de Sherbrooke, QC, Canada.

MOHAMMED-TAIFOUR, A., SCHWAAB, Q., PIOTON, J. & WEISS, J. 2015 A new wind tunnel for the study of pressure-induced separating and reattaching flows. *Aeronaut. J.* **119** (1211), 91–108.

MOHAMMED-TAIFOUR, A. & WEISS, J. 2016 Unsteadiness in a large turbulent separation bubble. *J. Fluid Mech.* **799**, 383–412.

MOKHTARI, S. & BRADSHAW, P. 1983 Longitudinal vortices in wind tunnel wall boundary layers. *Aeronaut. J.* **87** (866), 233–236.

NA, Y. & MOIN, P. 1998*a* Direct numerical simulation of a separated turbulent boundary layer. *J. Fluid Mech.* **374**, 379–405.

NA, Y. & MOIN, P. 1998*b* The structure of wall-pressure fluctuations in turbulent boundary layers with adverse pressure gradient and separation. *J. Fluid Mech.* **377**, 347–373.

OBI, S., AOKI, K. & MASUDA, S. 1993 Experimental and computational study of turbulent separating flow in an asymmetric plane diffuser. In *Ninth Symposium on Turbulent Shear Flows*, Kyoto, Japan, 16–18 August 1993.

PATRICK, W. P. 1987 Flowfield measurements in a separated and reattached flat plate turbulent boundary layer. *Tech. Rep.* NASA Contractor Report 4052. National Aeronautics and Space Administration.

PEARSON, D. S., GOULART, P. J. & GANAPATHISUBRAMANI, B. 2013 Turbulent separation upstream of a forward-facing step. *J. Fluid Mech.* **724**, 284–304.

PERRY, A. E. & FAIRLIE, B. D. 1975 A study of turbulent boundary-layer separation and reattachment. *J. Fluid Mech.* **69** (4), 657–672.

RAIESI, H., PIOMELLI, U. & POLLARD, A. 2011 Evaluation of turbulence models using direct numerical and large-eddy simulation data. *J. Fluids Engng* **133** (2), 021203.

RAJAEE, M., KARLSSON, S. K. F. & SIROVICH, L. 1994 Low-dimensional description of free-shear-flow coherent structures and their dynamical behaviour. *J. Fluid Mech.* **258**, 1–29.

SCHLICHTING, H. 1968 *Boundary Layer Theory*, 6th edn. McGraw-Hill.

SCHWAAB, Q. & WEISS, J. 2015 Evaluation of a thermal-tuft probe for turbulent separating and reattaching flows. *Trans. ASME: J. Fluids Engng* **137**, 011401.

SIMMONS, D., THOMAS, F. O. & CORKE, T. C. 2019 Smooth body flow separation experiments and their surface flow topology characterization. *AIAA Paper* 2019-3085.

SIMPSON, R. L. 1989 Turbulent boundary-layer separation. *Annu. Rev. Fluid Mech.* **21**, 205–234.

SIMPSON, R. L., GHODBANE, M & MCGRATH, B. E. 1987 Surface pressure fluctuations in a separating turbulent boundary layer. *J. Fluid Mech.* **177**, 167–186.

SKOTE, M. & HENNINGSON, D. S. 2002 Direct numerical simulation of a separated turbulent boundary layer. *J. Fluid Mech.* **471**, 107–136.

SPALART, P. R. & COLEMAN, G. N. 1997 Numerical study of a separation bubble with heat transfer. *Eur. J. Mech.* B/*Fluids* **16** (2), 169–189.

WEISS, J. 2019 A tutorial on the proper orthogonal decomposition. *AIAA Paper* 2019-3333.

WEISS, J., MOHAMMED-TAIFOUR, A. & SCHWAAB, Q. 2015 Unsteady behavior of a pressure-induced turbulent separation bubble. *AIAA J.* **53** (9), 2634–2645.

WEISS, J., SCHWAAB, Q., BOUCETTA, Y., GIANI, A., GUIGUE, C., COMBETTE, P. & CHARLOT, B. 2017 Simulation and testing of a MEMS calorimetric shear-stress sensor. *Sensors Actuators* **253**, 210–217.

WINANT, C. D. & BROWAND, F. K. 1974 Vortex pairing: the mechanism of turbulent mixing-layer growth at moderate Reynolds number. *J. Fluid Mech.* **63** (02), 237–255.

WU, W., MENEVEAU, C. & MITTAL, R. 2020 Spatio-temporal dynamics of turbulent separation bubbles. *J. Fluid Mech.* **883**, A45.

WU, W. & PIOMELLI, U. 2018 Effects of surface roughness on a separating turbulent boundary layer. *J. Fluid Mech.* **841**, 552–580.